WANG, Y., SUN, Y., WU, F., ZOU, G., GAUMET, J.-J., LI, J., FERNANDEZ, C., WANG, Y. and PENG, Q. 2024. Nitrogen-anchored boridene enables Mg–CO2 batteries with high reversibility. *Journal of the American Chemical Society* [online], 146(14), pages 9967–9974. Available from: https://doi.org/10.1021/jacs.4c00630

Nitrogen-anchored boridene enables Mg–CO2 batteries with high reversibility.

WANG, Y., SUN, Y., WU, F., ZOU, G., GAUMET, J.-J., LI, J., FERNANDEZ, C., WANG, Y. and PENG, Q.

2024

Nitrogen-Anchored Boridene Enables Mg−CO_2 Batteries with High Reversibility

Yangyang Wang, Yong Sun, Fengqi Wu, Guodong Zou,* Jean-Jacques Gaumet,
Jinyu Li, Carlos Fernandez, Yong Wang, and Qiuming Peng*

ABSTRACT: Nanoscale defect engineering plays a crucial role in incorporating extraordinary catalytic properties in two-dimensional materials by varying the surface groups or site interactions. Herein, we synthesized high-loaded nitrogen-doped Boridene (N-Boridene (Mo4/3(BnN1−n)2−mTz), N-doped concentration up to 26.78 at %) nanosheets by chemical exfoliation followed by cyanamide intercalation. Three different nitrogen sites are observed in N-Boridene, wherein the site of boron vacancy substitution mainly accounts for its high chemical activity. Attractively, as a cathode for Mg−CO2 batteries, it delivers a long-term lifetime (305 cycles), high-energy efficiency (93.6%), and ultralow overpotential (∼0.09 V) at a high current of 200 mA g−1, which overwhelms all Mg−CO2 batteries reported so far. Experimental and computational studies suggest that N-Boridene can remarkably change the adsorption energy of the reaction products and lower the energy barrier of the rate-determining step (*MgCO2 → *MgCO3·xH2O), resulting in the rapid reversible formation/decomposition of new MgCO3·5H2O products. The surging Boridene materials with defects provide substantial opportunities to develop other heterogeneous catalysts for efficient capture and converting of CO2.

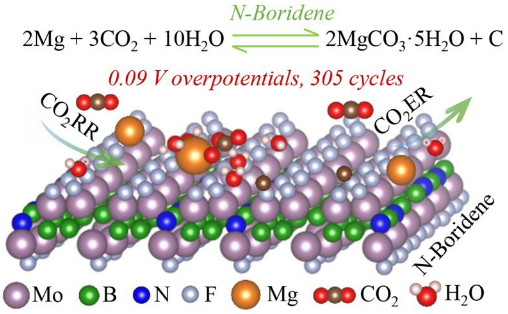

1. INTRODUCTION

Metal−CO_2 batteries, relative to the utilization and fixation of CO_2, are emerging as a typical "killing two birds with one stone" strategy, and economics of these batteries will handle the challenges of energy crises and the greenhouse effects.[1−4] Various rechargeable metal−CO_2 batteries with the anodes of comprising Li, Na, and K have been developed in the past decade.[5−7] Nevertheless, their high activities, dendrite formation, and high costs have restricted practical application.[8,9] Comparatively, the Mg candidate is anticipated to offer substantial improvements in the volumetric energy density and battery affordability, due to the use of earth-abundant, high-capacity, and dendrite-resistant Mg-metal anodes.[10−12] However, there are still several issues, including high polarization rate, slow redox reaction kinetics, and poor reversibility, for the Mg−CO_2 batteries. The fundamental reason is that the carbonate ($MgCO_3$) reaction product exhibits insulating properties and then makes C=O bonds virtually unbreakable, which decreases the electrochemical activity.[13−15]

Catalyst modification is an effective way to solve these issues by changing the discharge products.[16−20] The Mo_2C-based catalyst facilitates the generation of MgC_2O_4 in the Mg−CO_2 batteries.[13,21] However, undecomposed side products ($MgCO_3$, MgO) accumulate at the cathode, which increased the interfacial impedance, and slowed the carbon dioxide reduction reaction (CO_2RR) and carbon dioxide evolution reaction (CO_2ER) kinetics.[22] In addition, carbon nanotubes (CNTs) can induce the formation of $MgCO_3\cdot 3H_2O$ discharge products from Mg−CO_2 batteries in a moist CO_2 atmosphere, which allows for charging/discharging cycles.[23] Unfortunately, the CNTs cause the rapid failure of cycling performance and high overpotential in the batteries due to their poor catalytic capacities. Therefore, the development of efficient catalyst for the Mg−CO_2 batteries still remains a great challenge.

More recently, a new two-dimensional (2D) molybdenum boride (labeled Boridene), related to the normal composition of $Mo_{4/3}B_{2-x}T_z$ (where T_z is F, O or OH), can be prepared by selective etching of Y/Al atoms from the 3D in-plane chemically ordered MAB ($(Mo_{2/3}Y_{1/3})_2AlB_2$) phase in HF solutions.[24,25] Unlike carbon-based MXenes or graphene-typical materials,[26−28] this Boridene becomes more irregular due to the removing of two heterogeneous metallic atom layers, which results in the formation of a typical crumpled morphology with a large surface area.[29,30] More importantly, the B layer in Boridene has also been greatly destroyed because of the break of B−B bonds, resulting in a large number of macro-porous and microdefects.[31] In this regard, Boridene provides two important characteristics for the syntheses of various functional materials. On the one hand, differing from the C element ($2s^22p^2$), the B element with a $2s^22p^1$ electron structure can provide either empty orbit space or free-electron, displaying semiconducting, semimetallic, or metallic behavior.[32] On the other hand, Boridene possesses not only the ordered Y vacancies but also a plenty of unsaturated B sites, providing possible positions to anchor metallic or nonmetallic groups.

In the present work, we first fabricated nitrogen-doped Boridene (N-Boridene, $(Mo_{4/3}(B_nN_{1-n})_{2-m}T_z)$ nanosheets with a high N concentration of 26.78 at % through chemical exfoliation of MAB followed by cyanamide intercalation. Three different nitrogen sites have been identified, and the site of boron vacancy substitution is mainly attributed to its high reactivity. The N-Boridene catalyst used in Mg−CO_2 batteries g^{-1}) and an extremely low overpotential (~0.09 V), out-performing all hitherto reported Mg−CO_2 batteries.

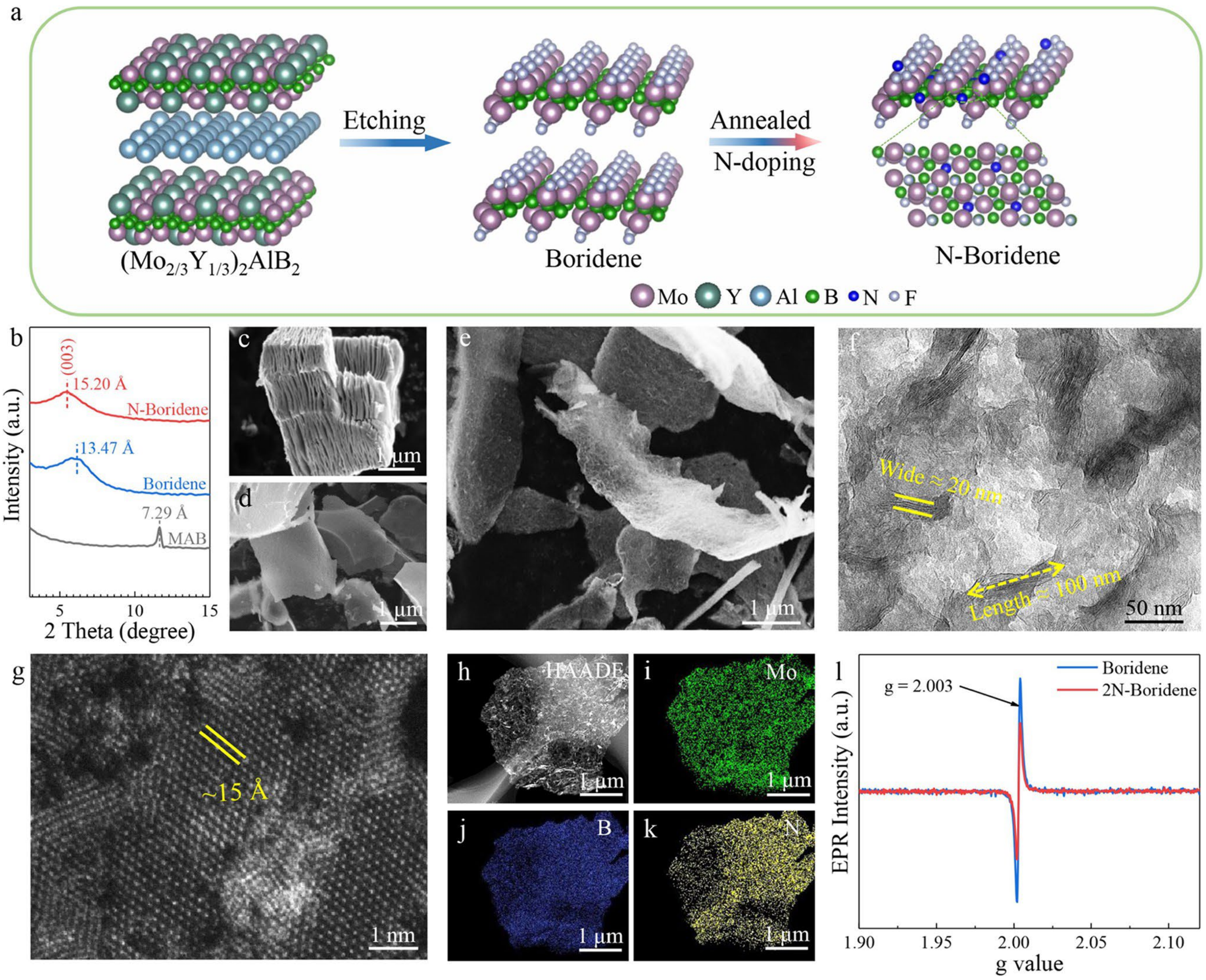

Figure 1. Structural characteristics of the N-Boridene. (a) Schematic diagram for preparing the N-Boridene. (b) XRD patterns of the MAB, Boridene, and N-Boridene, respectively. SEM images of (c) multilayer and (d) few-layer Boridene. (e) SEM, (f) TEM, (g) HRTEM, and (h−k) elemental mapping images of the N-Boridene, respectively. (l) EPR spectra of the Boridene and N-Boridene.

2. RESULTS AND DISCUSSION

A typical two-step method related to chemical exfoliation followed by cyanamide intercalation (Figure 1a) has been performed to prepare the crumpled N-Boridene compounds.[33−35] Specifically, the diffraction peaks of the MAB precursor completely disappeared after chemical exfoliation in a HF solution. As evidenced by the X-ray diffraction (XRD) patterns, the (000*l*) peak becomes broad and be reduced to a lower angle of $2\theta \approx 6.31°$ in the Boridene, in correspondence with the increased distance to 13.47 Å (Figures 1b and S1a). This chemical reaction has been confirmed as follows:[24] $(Mo_{2/3}Y_{1/3})_2AlB_2 + 5HF = AlF_3 + 2/3YF_3 + 5/2H_2 + Mo_{4/3}B_{2-x}T_x$. Subsequently, negatively charged Boridene nanosheets were conjugated with positively charged NH_2CN by electrostatic interactions. The resultant product was optimizes the reaction routes by forming the new discharge product $MgCO_3{\cdot}5H_2O$ in a moist CO_2 atmosphere and accelerates the charge transfer between the catalyst and product, achieving high cyclability (305 cycles at 200 mA annealed at 500 °C to fabricate the N-Boridene. This cyanamide intercalation process has been well identified with the shifting of (003) peak toward a lower angle, partially relative to the incorporation of N heteroatoms in the defective backbone of the Boridene.[36] Additionally, both scanning electron microscopy (SEM) and transmission electron microscopy (TEM) images show that the smooth several layer 2D sheets of the nanostructured $Mo_{4/3}B_{2-x}T_z$ have been successfully exfoliated from the densely layer-stacked structure of MAB (Figures 1c,d and S1b−e). As shown in the TEM and high-resolution TEM images (HRTEM, Figures 1e−g and S1d,e), some of the ordered vacancies, porous and point defects are homogeneously distributed in the N-Boridene.

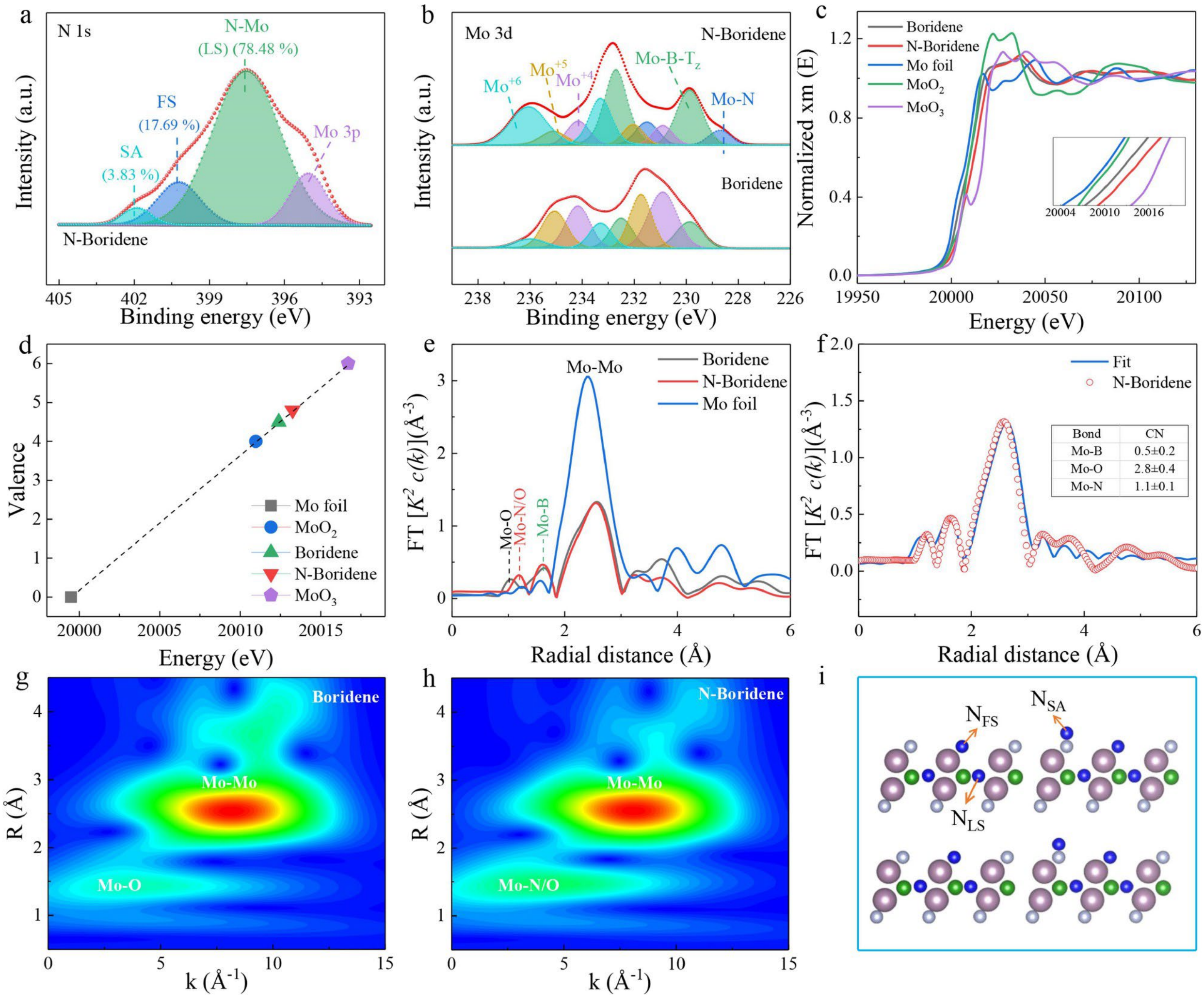

Bond	CN
Mo-B	0.5±0.2
Mo-O	2.8±0.4
Mo-N	1.1±0.1

Figure 2. Coordinated N doping. (a) High-resolution N 1s and (b) Mo 3d XPS spectra of the Boridene and the N-Boridene. (c) Normalized XANES spectra of Mo K-edge for the Mo foil, MoO_2, MoO_3, Boridene, and N-Boridene, respectively. (d) Fitted chemical valences for Mo atom in the Boridene and the N-Boridene. (e) Fourier-transformed Mo K-edge EXAFS spectra for the Mo foil, Boridene, and N-Boridene. (f) FT-EXAFS fitting curves of the N-Boridene. WT-EXAFS plots of (g) Boridene and (h) N-Boridene, respectively. (i) Schematic view of three N sites in the N- Boridene.

The average lateral size of the N-Boridene is ∼5 μm (Figure S 1f), and the length of the wrinkled nanobelts is ∼100 nm (Figure 1f). The lattice striation spacing of the N-Boridene is ∼15 Å, corresponding to the (003) plane, consistent with the XRD patterns (Figure 1b). According to the element mapping analysis (Figure 1h−k), the chemical composition is mainly composed of Mo, B, and N. Additionally, electron paramagnetic resonance (EPR) spectrum (Figure 1l) indicates that the intensity of the EPR signal at g = 2.003 for N-Boridene is two times lower than that in the Boridene, which tentatively justifies that the lack of vacancies possibly depends on the N atom domination.[37]

According to the X-ray photoelectron spectroscopy (XPS) combined with the inductively coupled plasma-optical emission spectroscopy (ICP-OES) results, the detailed chemical composition of the Boridene is $Mo_{4/3}B_{5/3}T_x$ (Table S2; Figure S2). Compared to the previous results, the ratio of Mo and B is similar and the morphology is the same, whereas the surface group fraction changes slightly.[29] To probe the N-doping structure, XPS measurements have been performed. Three different N-bonds (Figure 2a) are observed in the N-Boridene, relative to the lattice substitution of boron vacancy at 397.6 eV for N_{LS} (78.48%),[38,39] the function substitution at 400.2 eV for N_{FS}, and the surface absorption at 402.1 eV for N_{SA},[40] respectively.

Moreover, the N content in the N-Boridene is approximately 26.78 at %, which is the highest value among the 2D transition metal carbides or borides (Tables S1 and S3). Note that the peak at 394.9 eV can be classified as Mo $3p_{3/2}$, due to the peak position overlap between Mo 3p and N 1s.[41] In the case of the Mo peaks (Figure 2b), the new doublet peaks at 228.55 and 231.5 eV reveal the formation of Mo−N bonds in the N-Boridene.[39,41] Compared with the Boridene, the high-resolution B 1s peak (Figure S3b) shows the formation of B−N bond in the N-Boridene.[42] These strong chemical interactions between N with Mo or B have also been confirmed in the Fourier transform infrared spectrograms (Figure S3c).[43]

To further probe the coordination structure of Mo in the N-Boridene, we performed X-ray absorption near-edge spectra (XANES) of the Mo K-edge (Figure 2c). Specifically, the white-line intensity of the Mo k-edge indicates the threshold value of energy absorption (E0) of the N-Boridene (20013.3 eV) is slightly higher than that of the Boridene (20012.2 eV), indicating an increment in the higher oxidation state of Mo, with the order of Mo foil < MoO2 < Boridene < N-Boridene < MoO3. Additionally, the spectral shape for N-Boridene is similar to that of Boridene, but it is distinguished from those of the Mo foil, MoO_2, and MoO_3. The average chemical valence of the Boridene and N-Boridene is +4.48 and +4.81, respectively, according to the standard oxides of Mo^{4+}, Mo^{6+}, and Mo foils (Figure 2d).

In addition, the extended X-ray absorption fine structure (EXAFS) at Mo k-edge (Figure 2e) indicates that the N-Boridene show the higher peak intensity of Mo−N/O bond compared to the Boridene, signifying a greater average coordination number (CN) of the first Mo shell, relative to the decrease of unsaturated B sites.[44,45] Note that the position for Mo−Mo bonds is identical for all three samples, and the peak intensities follow by Mo foil > Boridene ≈ N-Boridene. This suggests that the CN of Mo−Mo is virtually unchanged, proving that N deposition is related to B vacancies rather than Mo vacancies. Moreover, the Mo−N/O bonds in N-Boridene have a longer central bond distance than those in Boridene, implying the formation of Mo−N nearest neighbor bonds within the Mo−B coordination sphere (Figure S4a−c). As shown in the fitting results (Figure 2f and Table S4), the CN of Mo−B/Mo−N (1.6 ± 0.3) in the N-Boridene is larger than that of Mo−B (0.5 ± 0.3) in the Boridene, while the CN of Mo−Mo remains unchanged in both samples. This proves the decrease in vacancy intensities can be directly attributed to the N compensation-induced increase in CN, suggesting that the N-doped atoms are refilled into the B vacancies.[37]

The wavelet transforms (WTs) obtained from the EXAFS oscillations show (Figures 2h,g and S4d−f) that the maximum WT intensity (8.2 A^{-1}) is the same for both the Boridene and N-Boridene (correlated with Mo−Mo bonds). This confirms that they have similar 2D layer structures. Concurrently, they are considerably different from those of Mo foils, MoO_2, and MoO_3.[46] Also, the Mo−B/N in the N-Boridene with a higher k value presents a higher intensity compared to the Boridene due to the increment of CN in Mo−B after N atoms doped into B vacancies. Thus, N-doped in multiscale-deficient Boridene might alter the coordination sites around Mo atoms, inevitably triggering charge delocalization and electronic circumstance optimization at the active sites.[45] Based on this analysis, a possible molecular model is deduced in Figure 2i, wherein it involves three possible doping positions for N atoms. As a result, this unique cyanamide intercalation process can be induced as follows:

$$Mo_{4/3}B_{5/3}T_x + NH_2CN \rightarrow Mo_{4/3}(B_nN_{1-n})_{2-m}T_z + H_2O + CO_2 \qquad (1)$$

Cyclic voltammetry (CV) tests manifest that the N-Boridene batteries exhibit a higher current density than the Boridene at the CO_2RR (1.05 V) and CO_2ER onset potential (1.70 V), respectively (Figure S5b). Furthermore, compared with those of the CNT and Boridene-based batteries, the N-Boridene-based batteries show the lowest polarization gap (0.05 V) during the first cycle at 100 mA g^{-1} in which the same trend has also been observed at other current densities, demonstrating excellent reversibility over a wide range (Figures 3a and S5e). Additionally, the N-Boridene exhibits the highest discharge capacity of 10,300 mA h g^{-1} with the cutoff potentials of 0.4 and 3.0 V under 100 mA g^{-1}, which is 3.1 times higher than the CNT, as well as 2.3 times stronger than the Boridene (Figure S5d).

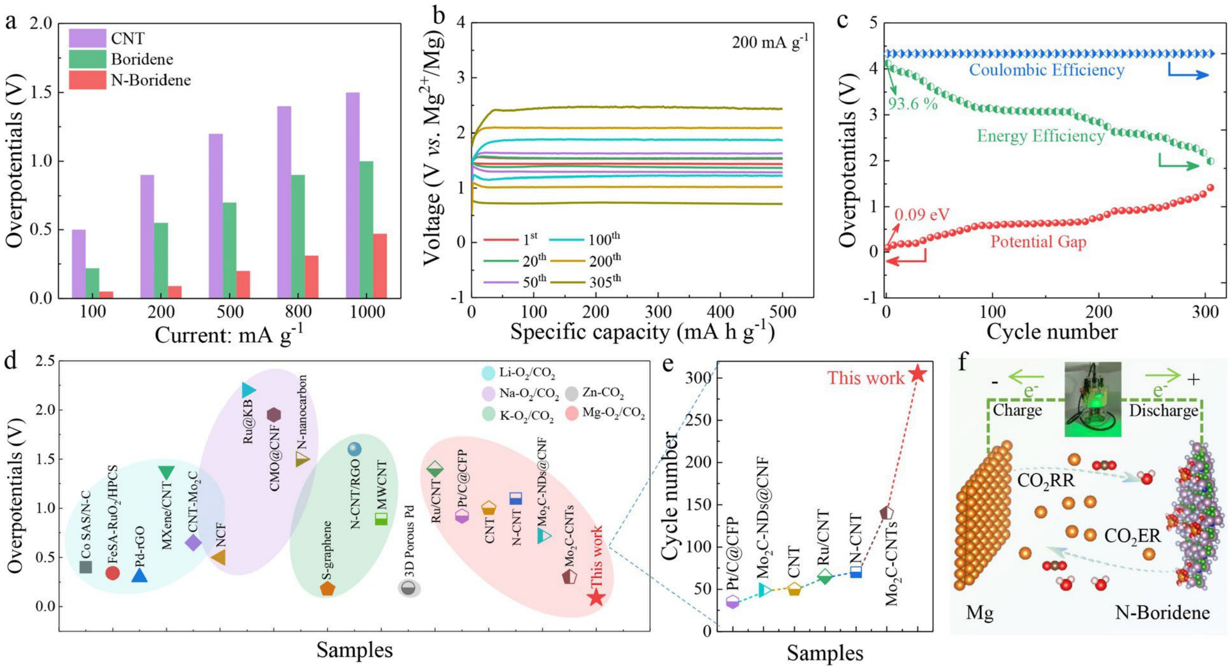

Figure 3. Electrocatalytic performances. (a) Comparison of the first-circle overpotentials for different catalysts as well as various current densities. (b) N-Boridene batteries at a current density of 200 mA g^{-1} with a controlled discharge/charge depth of 500 mA h g^{-1}. (c) Coulombic efficiency, energy efficiency, and overpotentials during 305 cycles. (d, e) Performance comparison with the previously reported overpotentials and cycle numbers. (f) Photo image of LED turned by the as-fabricated N-Boridene-based Mg−CO_2 batteries.

The variations in coulombic efficiency, energy efficiency, and polarization gap of the N-Boridene-based batteries are depicted in Figure 3b,c. The first cycle discharge voltage is 1.43 V, which remains at 1.22 V in the 100th cycle, with only 14.6% lose in the discharge potential. The continuous recycling measurements demonstrate a sustained coulombic efficiency of 100% over 305 cycles at a current density of 200 mA g$^{-1,}$ with an extremely low polarization gap (0.09 V) exhibited in the first cycle, accompanied by high energy efficiency (93.6%). The outstanding cycling properties of the N-Boridene-based Mg−CO_2 batteries have also been achieved under the different current densities together with various catalysts in terms of overpotentials, cycling revolutions, cycling time, specific capacities, and energy efficiency (Figures S5 and S6). Interestingly, the overpotential of the N-Boridene-based Mg−CO_2 battery holds a pivotal position among those of metal-O_2/CO_2 batteries (Figure 3d), while the cycling property falls among the superior candidates in Mg−O_2/CO_2 battery systems (Figure 3e). As shown in Figure 3f, a mode of Mg−CO_2 battery with LEDs lighting up in a humid CO2 environment confirms their potential practical applications.

To explore the Mg−CO_2 battery reaction process, different reactivity stages have been explored (discharge: A → C, charge: C → E, Figures S7 and S8) by an *in-situ* XRD method. In the case of the first discharge/charge period of the N-Boridene-based Mg−CO_2 batteries (Figure 4a), there are some new diffraction peaks gradually appearing at $2\theta \approx 12.3°$ and 24.4° during the discharge process, which can perfectly correlate to the (001) and (120) planes of the $MgCO_3{\cdot}5H_2O$, respectively. A gradual decrease and disappearance in the intensity of $MgCO_3{\cdot}5H_2O$ diffraction peaks was observed during the subsequent charging process. Simultaneously, as indicated by three-dimensional waterfall plots (Figure 4b), the $MgCO_3{\cdot}5H_2O$ peaks emerge during the discharge process and completely dissolve after the charging process, directly certifying the formation/decomposition of the $MgCO_3{\cdot}5H_2O$ product. In addition, uniform spherical discharge products with a diameter of ∼200 nm appear on the N-Boridene cathode surface (Figures 4c and S7d,e). The element mapping reveals a homogeneous distributions of C, Mg, and O elements. Moreover, the $MgCO_3{\cdot}5H_2O$ disappears and the cathode surface becomes smooth after charging. In contrast, the Boridene cathodes for Mg−CO2 batteries also generate spherical MgCO3·5H2O products after discharge; however, the diameter of product increases to 500 nm, and it cannot disappear completely after charging (Figure S9). The particle sizes of the discharge products are also affected by the water concentration (Figure S10). The suitable water concentration for the lowest MgCO3·5H2O dimension is 50 μL H2O. Note that the diameter of the discharge product grows to about 20 μm without water (Figure S11). Therefore, the reaction process can be summarized as follows:

$$2Mg + 3CO_2 + 10H_2O \leftrightarrow 2MgCO_3{\cdot}5H_2O + C \qquad (2)$$

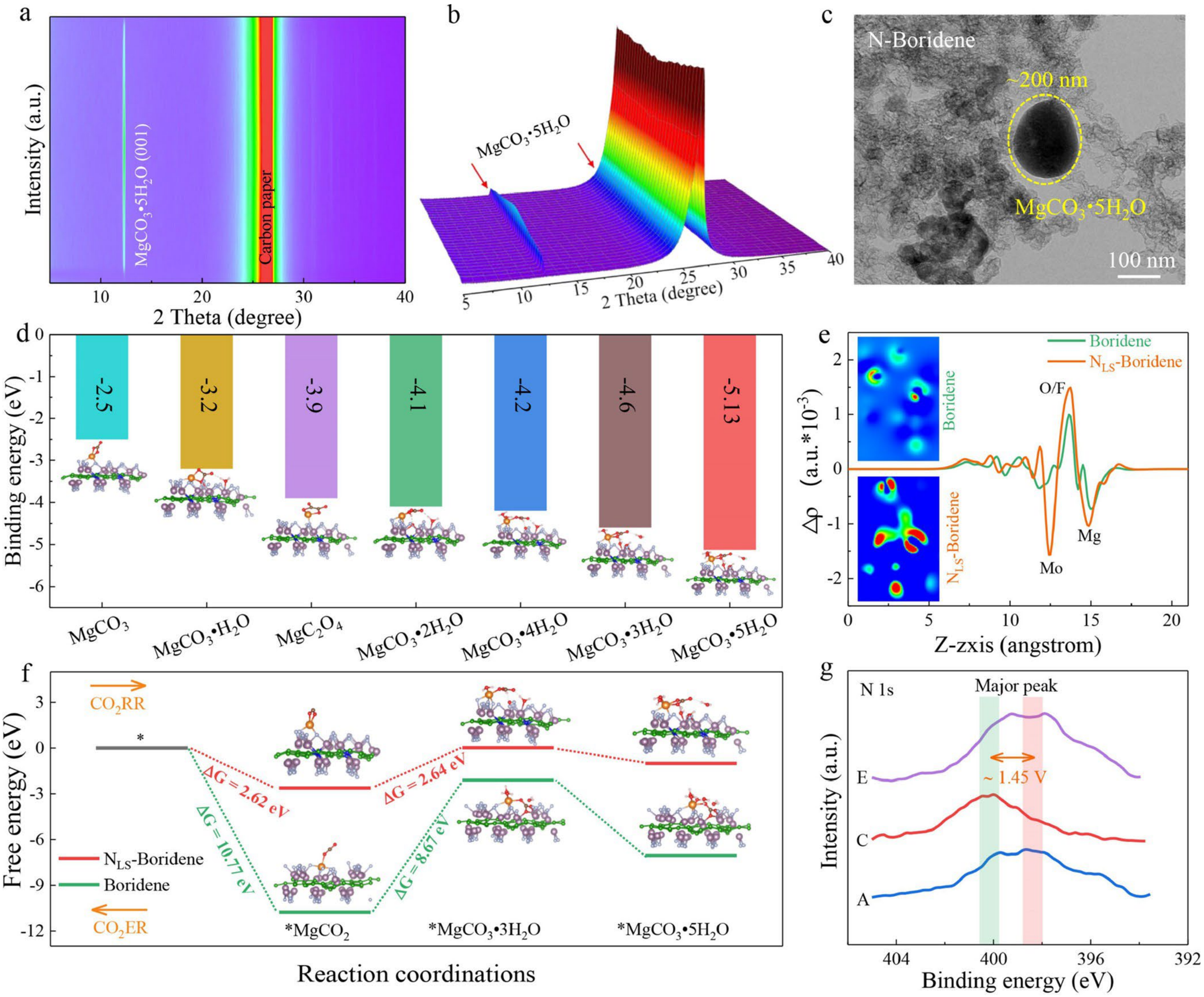

Figure 4. Reaction mechanisms. (a) In situ XRD contour mapping and (b) Three-dimensional falls distribution map during the first discharge/ charge process, respectively. (c) TEM image of $MgCO_3{\cdot}5H_2O$ during the first discharge process. (d) Adsorption energies of different discharge products on the N-Boridene substrate. (e) Electron transfer quantization ($\Delta\rho$) of $MgCO_3{\cdot}5H_2O$ by the Boridene and N-Boridene, respectively. The inset shows the charge transfer cross sections of Mg atoms on the Boridene and N-Boridene in the (010) direction. (f) Calculated free energy diagrams of different reaction intermediates on the active surfaces of the Boridene and N-Boridene, respectively. (g) XPS curves of N 1s during the first discharge/charge process.

Comparatively, in the case of the CNT-based Mg−CO_2 batteries, the discharge product mainly consists of $MgCO_3{\cdot}3H_2O$, and it fails to completely decompose after charging, which is in line with previous results (Figure S12).[23]

To clarify the efficiency of the catalytic N-Boridene, we performed density functional theory (DFT) calculations. In addition to the Boridene reference, three possible N positions in N-Boridene are explored (Figure S13), wherein it contains a homogeneous 2/3 metal Y vacancy, as well as a 1/3 nonmetal B vacancy.[29] The adsorption energy can be calculated as follows:[47]

$$E_a = \frac{1}{n}\left(E_{total} - n\cdot E_{slab} - \sum_i n_i E_{mi}\right) \tag{3}$$

where E_a is the adsorption energy, E_{total} is the total energy of the entire supercell containing the adsorbed object, the surface and possibly the periodic shear, E_{slab} is the energy of a pure surface, $\sum_i n_i E_{mi}$ is the total energy of the adsorbed object (molecule or atom), and n is the number of crystalline cells. Specifically, the magnitude of adsorption energy for the N_{LS}-Boridene is −5.13 eV toward the terminal discharge products ($MgCO_3 \cdot 5H_2O$) (Figure S14), which is far lower than those of other three structures (Boridene, N_{SA}-Boridene, N_{FS}-Boridene). According to the Sabatier principle,[48] this adsorption value is neither too strong nor too weak, and it is desirable for the good catalyst moieties. In this case, it is believed that the N_{LS}-Boridene structure plays a predominant role in the catalytic process, consistent with the highest fraction of N_{LS} (Figure 2a). Consequently, the following section focuses on evaluating the catalytic mechanisms for the formation of different reaction products on the N_{LS}-Boridene substrate.

In addition, the adsorption energies on the N_{LS}-Boridene catalyst for possible different discharge products, such as $MgCO_3$, MgC_2O_4, and $MgCO_3 \cdot xH_2O$, are calculated for the Mg−CO_2 batteries. Specifically, compared with those of the other six products, the binding energy of $MgCO_3 \cdot 5H_2O$ is the lowest, demonstrating its extraordinary superiority in the Mg−CO_2 batteries (Figures 4d and S15). Moreover, as evidenced by electron transfer quantization ($\Delta\rho$, Figures 4e and S16), the N-doping in the Boridene increases electron transfer along the Z-direction, in terms of the average planar charge density differences between the Boridene and N_{LS}-Boridene planes of $MgCO_3 \cdot 5H_2O$. Accordingly, the electron redistribution changes the electronic structure of catalyst surface, facilitating the ample electron gain/loss between catalyst and discharge product, which is also confirmed by the reversible shift of the N 1s XPS spectra during the discharge/charge process (Figure 4g). Moreover, the density of states (DOS) (Figure S17) shows the N_{LS}-Boridene with a better continuum and a larger total area compared with the Boridene, signifying a more high-speed electron transfer during the catalytic process.[49]

To further determine the possible reaction path, the free energies of different meditated reaction co-ordinations have been calculated. Figure 4f describes the possible reaction paths for the CO_2RR/CO_2ER process during the formation/ decomposition process of $MgCO_3 \cdot 5H_2O$. Specifically, the rate-determining step for the CO_2RR is the reduction of $^*MgCO_2$ to $^*MgCO_3 \cdot 3H_2O$, while the oxidation of $^*MgCO_2$ is the case for the CO_2ER process (Figure S18). The N_{LS}-Boridene exhibits both lower CO_2RR activation energy (2.64 eV) and CO_2ER activation energy (2.62 eV) compared with that of the Boridene. Intriguingly, the $^*MgCO_3 \cdot 3H_2O + 2H_2O \rightarrow {}^*MgCO_3 \cdot 5H_2O$ step for both catalysts is exothermic downhill processes, which occurs spontaneously under an ambient condition, providing partial evidence that the Boridene-based catalysts are preferential to form $MgCO_3 \cdot 5H_2O$. Furthermore, the decomposition phase in the bare Boridene ($^*MgCO_3 \cdot 5H_2O \rightarrow {}^*Mg + {}^*CO_2 + H_2O$) requires more energy. Conversely, this process is easier for the N_{LS}- Boridene, enabling its long-cycle behavior in combination with extremely low overpotentials.

3. CONCLUSIONS

Dependent on the strategy of defect-anchored atoms, we first synthesized a high-loaded N-doped Boridene nanosheet by chemical exfoliation followed by cyanamide intercalation. This unique N-Boridene catalyst effectively mitigates the poor cyclability problem of Mg−CO_2 batteries by selectively forming $MgCO_3 \cdot 5H_2O$ reaction products. Their stabilized cycle numbers and low overpotentials are far superior to those of the reported Mg−CO_2 batteries under the same conditions. Both experimental and theoretical results clarify that the N-Boridene assists the charge transfer between discharge product and substrate, which lowers the reaction energy barrier and accelerates the formation/decomposition of products, attributed to high cyclability, high energy efficiency, and remarkably low overpotential. Taking into account both various precursors and defect structures on the surface, a large number of different Boridene and its related derivatives will be prepared, which could provide more candidates for the development of electrochemical catalysts.

Corresponding Authors

Guodong Zou − *State Key Laboratory of Metastable Materials Science and Technology, Yanshan University, Qinhuangdao 066004, China*; Email: zouguodong@ ysu.edu.cn

Qiuming Peng − *State Key Laboratory of Metastable Materials Science and Technology, Yanshan University, Qinhuangdao 066004, China;* Email: pengqiuming@ysu.edu.cn

Authors

Yangyang Wang – *State Key Laboratory of Metastable Materials Science and Technology, Yanshan University, Qinhuangdao 066004, China*

Yong Sun – *State Key Laboratory of Metastable Materials Science and Technology, Yanshan University, Qinhuangdao 066004, China*

Fengqi Wu – *State Key Laboratory of Metastable Materials Science and Technology, Yanshan University, Qinhuangdao 066004, China*

Jean-Jacques Gaumet – *Laboratoire de Chimie et Physique, Approche Multi-échelles des Milieux Complexes, Institute Jean Barriol, Université de Lorraine, Metz 57070, France*

Jinyu Li – *State Key Laboratory of Metastable Materials Science and Technology, Yanshan University, Qinhuangdao 066004, China*

Carlos Fernandez – *School of Pharmacy and Life Sciences, Robert Gordon University, Aberdeen AB107GJ, U.K.*

Yong Wang – *College of Chinese Medicine, Beijing University of Chinese Medicine, Beijing 100029, China*

ACKNOWLEDGMENTS

We greatly acknowledge the financial support by National Natural Science Foundation (52171126, 52331003, and 52202374), "S&T Program of Hebei" (236Z1020G), the Hebei Natural Science Foundation (C2022203003, E2023203255, and E2022203167), Science Research Project of Hebei Education Department (BJK2024087), and Ministry of Education Yangtze River Scholar Professor Program of China (T2020124).

REFERENCES

(1) Jiao, K.; Xuan, J.; Du, Q.; Bao, Z.; Xie, B.; Wang, B.; Zhao, Y.; Fan, L.; Wang, H.; Hou, Z.; et al. Designing the Next Generation of Proton-Exchange Membrane Fuel Cells. *Nature* 2021, *595* (7867), 361–369.

(2) Chen, B.; Wang, D.; Tan, J.; Liu, Y.; Jiao, M.; Liu, B.; Zhao, N.; Zou, X.; Zhou, G.; Cheng, H.-M. Designing Electrophilic and Nucleophilic Dual Centers in the ReS_2 Plane toward Efficient Bifunctional Catalysts for Li-CO_2 Batteries. *J. Am. Chem. Soc.* 2022, *144* (7), 3106–3116.

(3) Mu, X.; Pan, H.; He, P.; Zhou, H. Li-CO_2 and Na-CO_2 Batteries: Toward Greener and Sustainable Electrical Energy Storage. *Adv. Mater.* 2019, *32* (27), No. 1903790.

(4) Tan, C.; Wang, A.; Cao, D.; Yu, F.; Wu, Y.; He, X.; Chen, Y. Unravelling the Complex Na_2CO_3 Electrochemical Process in Rechargeable Na-CO_2 Batteries. *Adv. Energy Mater.* 2023, *13* (13), No. 2204191.

(5) Shao, J.; Ao, H.; Qin, L.; Elgin, J.; Moore, C. E.; Khalifa, Y.; Zhang, S.; Wu, Y. Design and Synthesis of Cubic $K_{3-2x}Ba_xSbSe_4$ Solid Electrolytes for K-O_2 Batteries. *Adv. Mater.* 2023, *35* (48), No. 2306809.

(6) Lin, X.; Sun, Y.; Sun, Q.; Luo, J.; Zhao, Y.; Zhao, C.; Yang, X.; Wang, C.; Huo, H.; Li, R.; et al. Reviving Anode Protection Layer in Na-O_2 Batteries: Failure Mechanism and Resolving Strategy. *Adv. Energy Mater.* 2021, *11* (11), No. 2003789.

(7) Xia, C.; Kwok, C. Y.; Nazar, L. F. A High-Energy-Density Lithium-Oxygen Battery Based on a Reversible Four-Electron Conversion to Lithium Oxide. *Science* 2018, *361*, 777–781.

(8) Askins, E. J.; Zoric, M. R.; Li, M.; Amine, R.; Amine, K.; Curtiss, L. A.; Glusac, K. D. Triarylmethyl Cation Redox Mediators Enhance Li-O_2 Battery Discharge Capacities. *Nat. Chem.* 2023, *15* (9), 1247–1254.

(9) Ke, S.-W.; Li, W.; Gu, Y.; Su, J.; Liu, Y.; Yuan, S.; Zuo, J.-L.; Ma, J.; He, P. Covalent Organic Frameworks with Ni-Bis(dithiolene) and Co-Porphyrin Units as Bifunctional Catalysts for Li-O_2 Batteries. *Sci. Adv.* 2023, *9* (5), No. eadf2398.

(10) Muldoon, J.; Bucur, C. B.; Gregory, T. Quest for Nonaqueous Multivalent Secondary Batteries: Magnesium and Beyond. *Chem. Rev.* 2014, *114* (23), 11683–11720.

(11) Dong, H.; Liang, Y.; Tutusaus, O.; Mohtadi, R.; Zhang, Y.; Hao, F.; Yao, Y. Directing Mg-Storage Chemistry in Organic Polymers toward High-Energy Mg Batteries. *Joule* 2019, *3* (3), 782–793.

(12) Zhang, J.; Liu, J.; Wang, M.; Zhang, Z.; Zhou, Z.; Chen, X.; Du, A.; Dong, S.; Li, Z.; Li, G.; et al. The Origin of Anode-Electrolyte Interfacial Passivation in Rechargeable Mg-Metal Batteries. *Energy Environ. Sci.* 2023, *16* (3), 1111–1124.

(13) Liu, W.; Sui, X.; Cai, C.; Huang, H.; Xu, R.; Geng, D.; Chen, M.; Lu, J. A Nonaqueous Mg-CO_2 Battery with Low Overpotential. *Adv. Energy Mater.* 2022, *12* (34), No. 2201675.

(14) Zhao, W.; Yang, Y.; Deng, Q.; Dai, Q.; Fang, Z.; Fu, X.; Yan, W.; Wu, L.; Zhou, Y. Toward an Understanding of Bimetallic MXene Solid-Solution in Binder-Free Electrocatalyst Cathode for Advanced Li-CO_2 Batteries. *Adv. Funct. Mater.* 2022, *33* (5), No. 202210037.

(15) Cheng, Z.; Fang, Y.; Yang, Y.; Zhang, H.; Fan, Z.; Zhang, J.; Xiang, S.; Chen, B.; Zhang, Z. Hydrogen-Bonded Organic Framework to Upgrade Cycling Stability and Rate Capability of Li-CO_2 Batteries. *Angew. Chem., Int. Ed.* 2023, *62* (45), No. e202311480.

(16) Lu, J.; Jung Lee, Y.; Luo, X.; Chun Lau, K.; Asadi, M.; Wang, H.-H.; Brombosz, S.; Wen, J.; Zhai, D.; Chen, Z.; et al. A Lithium-Oxygen Battery Based on Lithium Superoxide. *Nature* 2016, *529* (7586), 377–382.

(17) Zhou, J.; Li, X.; Yang, C.; Li, Y.; Guo, K.; Cheng, J.; Yuan, D.; Song, C.; Lu, J.; Wang, B. A Quasi-Solid-State Flexible Fiber-Shaped Li-CO$_2$ Battery with Low Overpotential and High Energy Efficiency. *Adv. Mater.* 2018, *31* (3), No. 1804439.

(18) Yang, C.; Guo, K.; Yuan, D.; Cheng, J.; Wang, B. Unraveling Reaction Mechanisms of Mo$_2$C as Cathode Catalyst in a Li-CO$_2$ Battery. *J. Am. Chem. Soc.* 2020, *142* (15), 6983–6990.

(19) Qi, G.; Zhang, J.; Chen, L.; Wang, B.; Cheng, J. Binder-Free MoN Nanofibers Catalysts for Flexible 2-Electron Oxalate-Based Li- CO$_2$ Batteries with High Energy Efficiency. *Adv. Funct. Mater.* 2022, *32* (22), No. 2112501.

(20) Hou, Y.; Wang, J.; Liu, L.; Liu, Y.; Chou, S.; Shi, D.; Liu, H.; Wu, Y.; Zhang, W.; Chen, J. Mo$_2$C/CNT: An Efficient Catalyst for Rechargeable Li-CO$_2$ Batteries. *Adv. Funct. Mater.* 2017, *27* (27), No. 1700564.

(21) Liu, W.; Wang, N.; Wu, Y.; Zhang, Q.; Chen, X.; Li, Y.; Xu, R. High-Rate Nonaqueous Mg-CO$_2$ Batteries Enabled by Mo$_2$C-Nanodot-Embedded Carbon Nanofibers. *Small* 2023, *20*, No. 2306576.

(22) Peng, C.; Xue, L.; Zhao, Z.; Guo, L.; Zhang, C.; Wang, A.; Mao, J.; Dou, S.; Guo, Z. Boosted Mg-CO$_2$ Batteries by Amine-Mediated CO$_2$ Capture Chemistry and Mg^{2+}-Conducting Solid-electrolyte Interphases. *Angew. Chem., Int. Ed.* 2023, *63*, No. e202313264.

(23) Zhang, C.; Wang, A.; Guo, L.; Yi, J.; Luo, J. A Moisture-Assisted Rechargeable Mg-CO$_2$ Battery. *Angew. Chem., Int. Ed.* 2022, *61* (17), No. e202200181.

(24) Zhou, J.; Palisaitis, J.; Halim, J.; Dahlqvist, M.; Tao, Q.; Persson, I.; Hultman, L.; Persson, P. O. Å.; Rosen, J. Boridene: Two-Dimensional Mo$_{4/3}$B$_{2-x}$ with Ordered Metal Vacancies Obtained by Chemical Exfoliation. *Science* 2021, *373*, 801–805.

(25) Chen, J.; Lin, Y.; Wang, H.; Li, J.; Liu, S.; Lee, J. M.; Zhao, Q. 2D Molybdenum Compounds for Electrocatalytic Energy Conversion. *Adv. Funct. Mater.* 2022, *33* (4), No. 2210236.

(26) VahidMohammadi, A.; Rosen, J.; Gogotsi, Y. The World of Two-Dimensional Carbides and Nitrides (MXenes). *Science* 2021, *372* (6547), No. eabf1581.

(27) Li, Y.; Shao, H.; Lin, Z.; Lu, J.; Liu, L.; Duployer, B.; Persson, P. O. Å.; Eklund, P.; Hultman, L.; Li, M.; et al. A General Lewis Acidic Etching Route for Preparing MXenes with Enhanced Electrochemical Performance in Non-aqueous Electrolyte. *Nat. Mater.* 2020, *19* (8), 894–899.

(28) Wu, J.; Lin, H.; Moss, D. J.; Loh, K. P.; Jia, B. Graphene Oxide for Photonics Electronics and Optoelectronics. *Nat. Rev. Chem.* 2023, *7* (3), 162–183.

(29) Helmer, P.; Halim, J.; Zhou, J.; Mohan, R.; Wickman, B.; Björk, J.; Rosen, J. Investigation of 2D Boridene from First Principles and Experiments. *Adv. Funct. Mater.* 2022, *32* (14), No. 2109060.

(30) Hou, Y.; Chen, Z.; Li, X.; Wang, Y.; Li, P.; Cui, H.; Zhang, R.; Yang, S.; Zhang, S.; Zhi, C. MBene Promoted Zn Peroxide Chemistry in Rechargeable Near-Neutral Zn-Air Batteries. *Energy Environ. Sci.* 2023, *16* (8), 3407–3415.

(31) Clua-Provost, T.; Durand, A.; Mu, Z.; Rastoin, T.; Fraunié, J.; Janzen, E.; Schutte, H.; Edgar, J. H.; Seine, G.; Claverie, A.; et al. Isotopic Control of the Boron-Vacancy Spin Defect in Hexagonal Boron Nitride. *Phys. Rev. Lett.* 2023, *131* (12), No. 126901.

(32) Nair, V. G.; Birowska, M.; Bury, D.; Jakubczak, M.; Rosenkranz, A.; Jastrzębska, A. M. 2D MBenes: A Novel Member in the Flatland. *Adv. Mater.* 2022, *34* (23), No. 2108840.

(33) Li, M.; Lu, J.; Luo, K.; Li, Y.; Chang, K.; Chen, K.; Zhou, J.; Rosen, J.; Hultman, L.; Eklund, P.; et al. Element Replacement Approach by Reaction with Lewis Acidic Molten Salts to Synthesize Nanolaminated MAX Phases and MXenes. *J. Am. Chem. Soc.* 2019, *141* (11), 4730–4737.

(34) Bao, W.; Liu, L.; Wang, C.; Choi, S.; Wang, D.; Wang, G. Facile Synthesis of Crumpled Nitrogen-Doped MXene Nanosheets as a New Sulfur Host for Lithium-Sulfur Batteries. *Adv. Energy Mater.* 2018, *8* (13), No. 1702485.

(35) Yoon, Y.; Lee, M.; Kim, S. K.; Bae, G.; Song, W.; Myung, S.; Lim, J.; Lee, S. S.; Zyung, T.; An, K. S. A Strategy for Synthesis of Carbon Nitride Induced Chemically Doped 2D MXene for High-Performance Supercapacitor Electrodes. *Adv. Energy Mater.* 2018, *8* (15), No. 1703173.

(36) Fan, Z.; Wei, C.; Yu, L.; Xia, Z.; Cai, J.; Tian, Z.; Zou, G.; Dou, S. X.; Sun, J. 3D Printing of Porous Nitrogen-Doped Ti$_3$C$_2$ MXene Scaffolds for High-Performance Sodium-Ion Hybrid Capacitors. *ACS Nano* 2020, *14* (1), 867–876.

(37) Cui, Y.; Xiao, K.; Bedford, N. M.; Lu, X.; Yun, J.; Amal, R.; Wang, D. W. Refilling Nitrogen to Oxygen Vacancies in Ultrafine Tungsten Oxide Clusters for Superior Lithium Storage. *Adv. Energy Mater.* 2019, *9* (37), No. 1902148.

(38) Shi, X; Wu, A; Yan, H; Zhang, L.; Tian, C.; Wang, L.; Fu, H. A "MOFs plus MOFs" Strategy toward Co-Mo$_2$N Tubes for Efficient Electrocatalytic Overall Water Splitting. *J. Mater. Chem. A* 2018, *6* (41), 20100–20109.

(39) Guo, D.; Zhang, X.; Liu, M.; Yu, Z.; Chen, X. a.; Yang, B.; Zhou, Z.; Wang, S. Single Mo-N$_4$ Atomic Sites Anchored on N-Doped Carbon Nanoflowers as Sulfur Host with Multiple Immobilization and Catalytic Effects for High-Performance Lithium- Sulfur Batteries. *Adv. Funct. Mater.* 2022, *32* (35), No. 2204458.

(40) Lu, C.; Yang, L.; Yan, B.; Sun, L.; Zhang, P.; Zhang, W.; Sun, Z. Nitrogen-Doped Ti$_3$C$_2$ MXene: Mechanism Investigation and Electrochemical Analysis. *Adv. Funct. Mater.* 2020, *30* (47), No. 2000852.

(41) Wei, H.; Wang, J.; Lin, Q.; Zou, Y.; Chen, X. a.; Zhao, H.; Li, J.; Jin, H.; Lei, Y.; Wang, S. Incorporating Ultra-Small N-Doped Mo$_2$C Nanoparticles onto 3D N-Doped Flower-Like Carbon Nanospheres for Robust Electrocatalytic Hydrogen Evolution. *Nano Energy* 2021, *86*, No. 106047.

(42) Ji, X.; Liu, X.; Guo, Y.; Zhang, J. Developing Visible Light Responsive Z-scheme BN-PDI Photocatalysts with Good Degradation Performance for Antibiotics. *Chem. Eng. J.* 2021, *425*, No. 131260.

(43) Feng, L.; Zhang, L.; Zhang, S.; Chen, X.; Li, P.; Gao, Y.; Xie, S.; Zhang, A.; Wang, H. Plasma-Assisted Controllable Doping of Nitrogen into MoS$_2$ Nanosheets as Efficient Nanozymes with Enhanced Peroxidase-Like Catalysis Activity. *ACS Appl. Mater. Interfaces* 2020, *12* (15), 17547–17556.

(44) Wang, T.; Luo, D.; Zhang, Y.; Zhang, Z.; Wang, J.; Cui, G.; Wang, X.; Yu, A.; Chen, Z. Hierarchically Porous Ti$_3$C$_2$ MXene with Tunable Active Edges and Unsaturated Coordination Bonds for Superior Lithium-Sulfur Batteries. *ACS Nano* 2021, *15* (12), 19457– 19467.

(45) Wang, P.; Zhao, D.; Hui, X.; Qian, Z.; Zhang, P.; Ren, Y.; Lin, Y.; Zhang, Z.; Yin, L. Bifunctional Catalytic Activity Guided by Rich Crystal Defects in Ti_3C_2 MXene Quantum Dot Clusters for Li-O_2 Batteries. *Adv. Energy Mater.* 2021, *11* (32), No. 2003069.

(46) Dessie, T. A.; Huang, W.-H.; Adam, D. B.; Awoke, Y. A.; Wang, C.-H.; Chen, J.-L.; Pao, C.-W.; Habtu, N. G.; Tsai, M.-C.; Su, W.-N.; et al. Efficient H_2 Evolution Coupled with Anodic Oxidation of Iodide over Defective Carbon-Supported Single-Atom Mo-N_4 Electro- catalyst. *Nano Lett.* 2022, *22* (18), 7311–7317.

(47) Gao, W.; Chen, Y.; Li, B.; Liu, S.-P.; Liu, X.; Jiang, Q. Determining the Adsorption Energies of Small Molecules with the Intrinsic Properties of Adsorbates and Substrates. *Nat. Commun.* 2020, *11* (1), 1196.

(48) Hu, S.; Li, W.-X. Sabatier Principle of Metal-Support Interaction for Design of Ultrastable Metal Nanocatalysts. *Science* 2021, *374* (6573), 1360–1365.

(49) Zeng, H.; Li, Z.; Li, G.; Cui, X.; Jin, M.; Xie, T.; Liu, L.; Jiang, M.; Zhong, X.; Zhang, Y.; et al. Interfacial Engineering of TiO_2/Ti_3C_2 MXene/Carbon Nitride Hybrids Boosting Charge Transfer for Efficient Photocatalytic Hydrogen Evolution. *Adv. Energy Mater.* 2021, *12* (1), No. 2102765.

Supporting information

Nitrogen-Anchored Boridene Enables Mg-CO_2 Batteries with High Reversibility

Yangyang Wang,[†] Yong Sun,[†] Fengqi Wu,[†] Guodong Zou,*[,†] Jean-Jacques Gaumet,[‡] Jinyu Li,[†] Carlos Fernandez,[§] Yong Wang,[#] Qiuming Peng*[,†]

[†]State Key Laboratory of Metastable Materials Science and Technology, Yanshan University, Qinhuangdao, 066004, China;

[‡]Laboratoire de Chimie et Physique: Approche Multi-échelles,des Milieux Complexes (LCP-A2MC), Institute Jean Barriol, Université de Lorraine, Metz 57070, France;

[§]School of Pharmacy and life sciences, Robert Gordon University, Aberdeen, AB107GJ, U.K;

[#]College of Chinese Medicine, Beijing University of Chinese Medicine, Beijing 100029, China

*Corresponding Authors: zouguodong@ysu.edu.cn, pengqiuming@ysu.edu.cn

Table of Content

S1. Experimental section

S1.1 Chemicals and materials.

Mo (99.999%), Y (99.99%), Al (99.99%) and B (99.99%) were bought from Innochem Reagent (Shanghai) Co., Ltd., China. Chemicals, including hydrofluoric acid (HF, 40 wt %), cyanamide (CH_2N_2, 50 wt % in H_2O), $MgCl_2$ (99.9 %), etc., were purchased from Aladdin Reagent (Shanghai) Co., Ltd., China. All the chemicals and materials were used without further decontamination.

S1.2 Synthesis of 3D $(Mo_{2/3}Y_{1/3})_2AlB_2$ (MAB) phase.

MAB precursors have been prepared by an ultrahigh melting method. Specifically, the powders of the commercial elements obtained by stoichiometric molar ratio weighing (Mo:Y:B:Al = 4:2:6:1.4) were thoroughly mixed by mechanical ball milling at 400 rpm for 48 h. Then it was wrapped with Ta foil and inserted into a BN crucible in a cubic-anvil large-volume press with six rams. The loading pressure (5 GPa) was added before increasing the temperature. The temperatures varied from room temperature to 1400 °C and held for 30 min. After cooling to room temperature, the loosely sintered samples were crushed and sieved through a 400 mesh screen to obtain MAB powders.

S1.3 2D Boridene ($Mo_{4/3}B_{2-x}T_z$).

Two dimensional (2D) Boridene was prepared by selective etching the Al and Y atoms from $(Mo_{2/3}Y_{1/2})_2AlB_2$. Briefly, 2.0 g $(Mo_{2/3}Y_{1/2})_2AlB_2$ was slowly added to a Teflon beaker (50 mL) with 20 mL HF and held at 0 ℃ for 15 min， then transferred to a silicone oil bath and magnetically stirred at 35 ℃ for 18 h. After etching, the obtained etched product was repeatedly centrifuged (5000 rpm/5 min) and washed with deionized water until the pH approached 7. For further delamination, the obtained multi-layer $Mo_{4/3}B_{2-x}T_z$ Boridene was dispersed in 10 mL 1M of TMAOH and stirred for 2 h at room temperature. Then, the sample was centrifuged at 8000 rpm for 3 min and washed three times with ethanol to remove the residual TMAOH. Finally, 15 mL deionized water was added to the powder which was shaken for 10 min to obtain single-layer $Mo_{4/3}B_{2-x}T_z$ sheets. The mixture was then centrifuged at 3500 rpm for 10 min to remove un-delaminated crystals, and the final colloidal suspension of delaminated $Mo_{4/3}B_{2-x}T_z$ sheets was collected for further characterization, with an obtained average concentration of the suspension of about 2.0 mg/mL.

S1.4 Fabrication of the crumpled N-Boridene.

50 mL of delaminated Boridene colloidal suspensions was mixed with 0.4 g of cyanamide (50 wt%) dissolved in 50 mL 0.1 M dilute hydrochloric acid (protonation) in a weight ratio of Boridene to cyanamide of 1:1. Boridene was generally negatively charged due to their functional groups (e.g., -O, -F and -OH) on the surface, therefore positively charged cyanamide was adsorbed onto the negatively charged surface of delaminated Boridene due to the electrostatic interactions during mixing. Upon centrifugation and freeze-drying, the product was annealed at 500 ℃ in an Ar ambient for 2 h to attain the crumpled nitrogen-doped Boridene (named N-Boridene).

S1.5 Material characterization.

The phase purity and crystal structure of the samples were recorded on an X-ray diffractometer (Rigaku D/MAX-2005/PC) using Cu K*a* radiation (λ = 1.5406 Å) with a step scan of 0.02 degree per step and a scan rate of 3 degree/min. SEM was conducted with a Hitachi S-4800. Transmission electron microscope (TEM) images were observed on a Titan ETEM G2 at 300 kV. ICP-MS was measured by Agilent 7700/7800 (Agilent Technologies Co. Ltd., USA). FT-IR spectrometers were investigated by Nexus 870 (Thermo SCIENTIFIC, USA). Raman was obtained from inVia Qontor (Renishaw England). X-ray absorption fine structure (XAFS) spectra of the Mo K-edge were conducted at room temperature from the beamline BL07A1 in National Synchrotron Radiation Research Center (NSRRC). The radiation was monochro-matized by a Si (111) double-crystal monochromator. The acquired EXAFS data were processed according to the standard procedures using the ATHENA module implemented in the IFEFFIT software packages. XANES and EXAFS data reduction and analysis were processed by Athena software. X-ray photoelectron spectroscopy (XPS) was conducted on a ThermoFisher with Al Kα (1486.71 eV) X-ray radiation (15 kV and 10 mA). The binding energies obtained in the XPS analysis were corrected by referencing the C 1s peak position (284.80 eV).

S1.6 Electrochemical measurements.

The cathode was prepared by mixing Ketjenblack, N-Boridene and PVDF in the weight ratio of 6:3:1 in N-methylpyrrolidinone (NMP) to obtain a homogeneous slurry, followed by coating on carbon paper. The catalysts coating was 0.2-0.25 mg cm^{-2}. The CR2032 coin-type Mg-CO_2 battery composed of a Mg foil anode (15.6 mm in diameter), a glass fiber filter separator (Whatman, GF/A), an electrolyte (0.5 M

$MgCl_2$ and 0.25 M magnesium bis(trifluoromethane) sulfonamide ($Mg(TFSI)_2$) in 1, 2-dimethoxyethane (DME) solution), and an air cathode (N-Boridene: 12 mm in diameter), were assembled in an argon-filled glove box. The assembled battery was then placed in a 250 mL glass container filled with high purity CO_2 (99.999 %, 1.0 atm) and 50 μL of water was added to the bottle for evaporation. A vial containing 5 mL of DME was also placed to avoid running out of solvent. The final test was carried out after 8 h of resting.

All potentials were referenced against Mg^{2+}/Mg. The galvanostatic discharge/charge tests were collected on a LAND CT3002A battery test instrument. CVs were conducted on a BioLogic VMP3 electrochemical workstation in the potential window of 0.4-3.0 V, and the scan rate was 0.2 mV s^{-1}.

S1.7 Theoretical calculations.

All calculations were performed based on DFT as implemented in the Vienna ab initio simulation package (VASP) with the projector-augmented-plane-wave method.[1-2] Electron spin polarization was considered in all calculations. The exchange-correlation interaction was treated with the generalized gradient approximation of Perdew-Burke-Ernzerhof,[3] while DFT+D3 was used for handling weak interactions.[4] The cut-off energy for the plane-wave basis was 450 eV, and a Monkhorst-Pack K-points were 2×2×1 in the Brillouin zone. The lattice constants and internal coordinates were optimized until the atomic forces become less than 10^{-4} eV/Å. Energy and maximum stress were converged to 10^{-5} eV and 0.05 eV/Å, respectively.

The overall chemical reactions for generating $MgCO_3 \cdot 5H_2O$ were described as

$$2Mg + 3/2CO_2 + 5H_2O \leftrightarrow MgCO_3 \cdot 5H_2O + 1/2C \qquad (1)$$

The change of the free energy (ΔG) in the reaction was calculated considering zero point energy corrections (ZPE) and entropy change ($T\Delta S$) from the vibrational frequencies associated with the normal modes in the harmonic approximation.

S2. Supporting tables.

Table S1. The atomic concentration (at %) for the different elements from MAB, Boridene, N-Boridene, respectively.

Sample	Concentration / at %							
	Mo	Y	C	Al	B	O	N	F
MAB	6.46	6.23	20.47	6.39	17.92	42.53	--	--
Boridene	7.68	0.48	34.15	0.1	18.86	35.35	--	3.38
N-Boridene	7.67	--	19.51	--	21.89	23.94	26.78 (18.3 wt %)	0.21

Table S2. Comparison of ICP content of Mo and B elements in Boridene and N-Boridene, separately.

Samples	Elements	Weight (g)	Composition (mg/L)	Mass fraction (wt %)
Boridene	Mo	0.0291	10.289	44.1976
	B	0.0291	1.3823	5.9378
N-Boridene	Mo	0.0341	14.437	52.9201
	B	0.0341	1.6099	5.9012

Table S3. Nitrogen contents in the different two-dimensional MXene materials.

Samples	N content (at %)	Reference
N-doped porous MXene/TiO_2	1.67	[5]
2.5-N-MXene	2.50	[6]
Ti_3C_2-$CT_{confined}$	3.63	[7]
$Ti_3C_2T_x$-N_6	5.00	[8]
Pd/N-B-Ti_3C_2	6.29	[9]
N-Ti_3C_2(H)	7.10	[10]
Porous N-$Ti_3C_2T_x$	8.41	[11]
Ti_3C_2-PND	9.10	[12]
N-$Ti_3C_2T_x$	11.52	[13]
900N-Ti_2CT_x	15.48	[14]
M8T1	19.26	[15]
N-$Ti_3C_2T_x$-700 ℃	20.70	[16]
N-Boridene	**26.78**	**-**

Table S4. Corresponding fit parameters for the Boridene and N-Boridene.

Samples	shell	CN	R(Å)	δ^2(Å^2)
Mo foil	Mo-Mo1	8	2.71	0.003
	Mo-Mo2	6	3.13	0.002
Boridene	Mo-O	2.8±0.3	1.05	0.008
	Mo-B	0.5±0.3	1.62	0.001
	Mo-Mo1	4.9±0.3	2.66	0.005
	Mo-Mo2	3.4±0.6	3.10	0.005
N-Boridene	Mo-O	2.8±0.4	1.04	0.012
	Mo-N	1.1±0.1	1.18	0.003
	Mo-B	0.5±0.2	1.64	0.001
	Mo-Mo1	5.7±0.3	2.66	0.008
	Mo-Mo2	1.9±0.2	3.07	0.001

Table S5. Overpotentials for the different metal-CO_2 batteries.

Batteries	Cathode materials	Overpotential
Li-O_2	Co SA_S/N-C[17]	0.40
Li-O_2	Fe_{SA}-RuO_2/HPCS[18]	0.34
Li-O_2	Pd-rGO[19]	0.30
Li-CO_2	MXene/CNT[20]	1.38
Li-CO_2	CNT-Mo_2C[21]	0.65
Na-O_2	NCF[22]	0.50
Na-CO_2	Ru@KB[23]	2.20
Na-CO_2	CMO@CNF[24]	1.95
Na-CO_2	N-nanocarbon[25]	1.50
K-O_2	S-graphene[26]	0.18
K-CO_2	N-CNT/RGO[27]	1.60
K-CO_2	MWCNT[28]	0.89
Zn-CO_2	3D Porous Pd[29]	0.19
Mg-O_2	Ru/CNT[30]	1.40
Mg-O_2	Pt/C@CFP[31]	0.92
Mg-CO_2	CNT[32]	1.00
Mg-CO_2	Mo_2C-NDs@CNF[33]	0.72
Mg-CO_2	Mo_2C-CNTs[34]	0.30
This work	**N-Boridene**	**0.09**

3. Supporting figures.

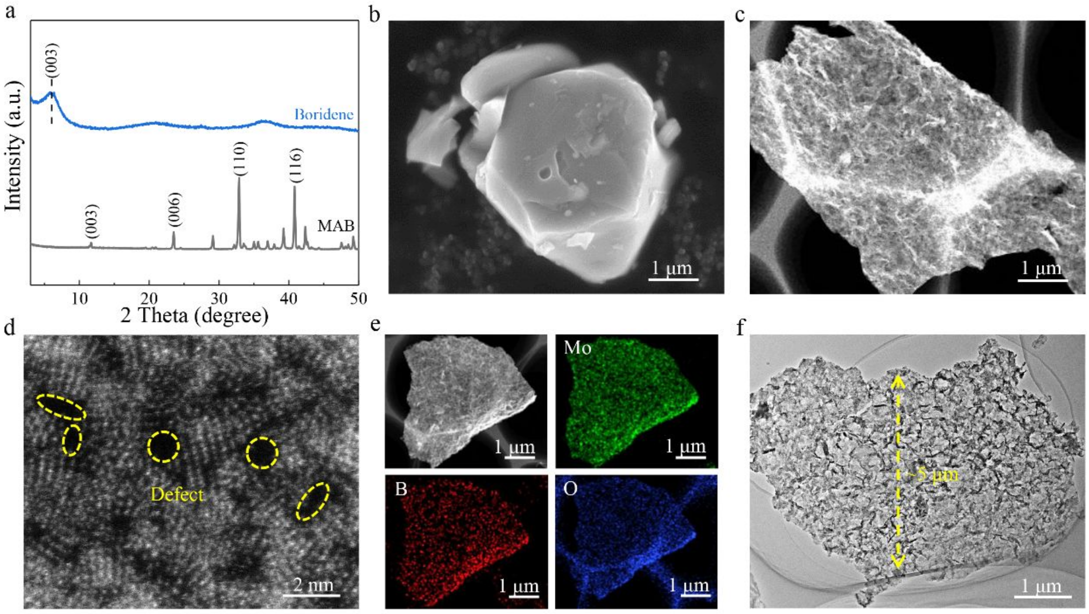

Figure S1. (a) XRD for the MAB and Boridene. (b) SEM for the MAB. (c) TEM, (d) HRTEM and (e) elemental mapping for the Boridene, individually. (f) TEM for the N-Boridene.

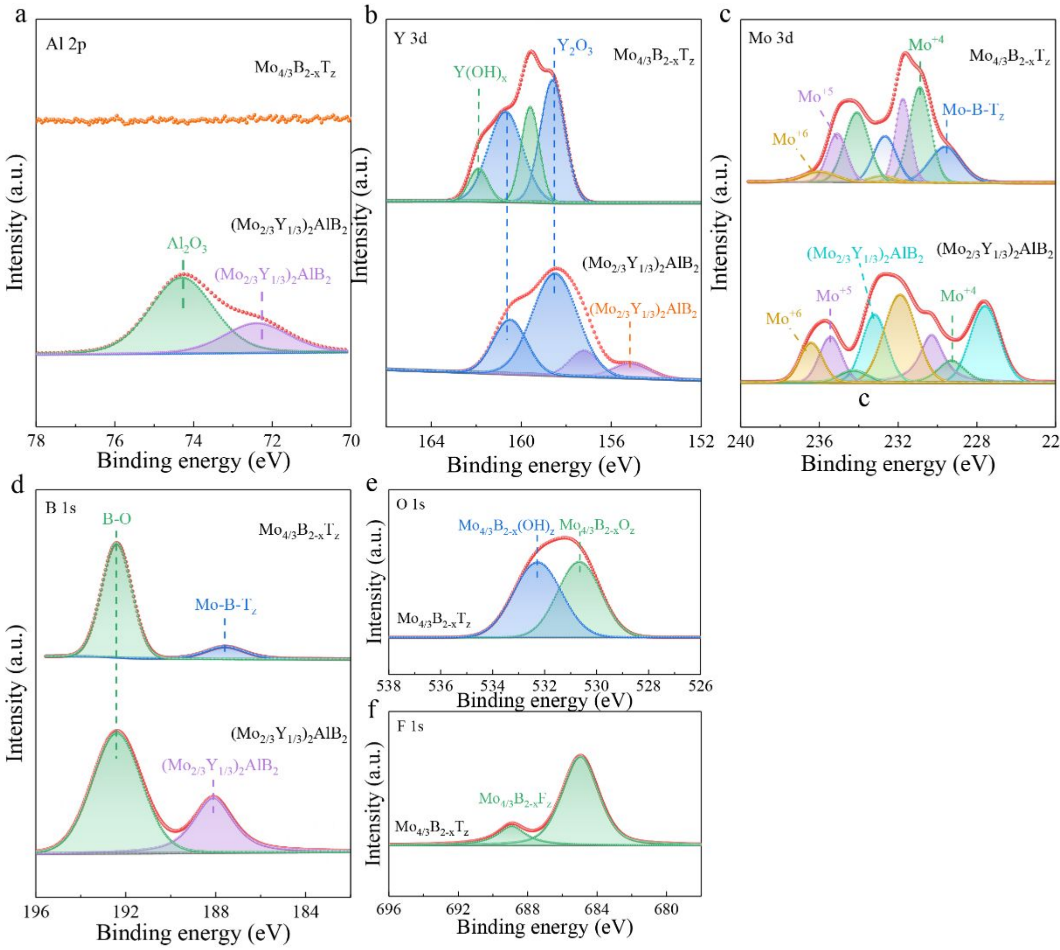

Figure S2. XPS high-resolution diagrams of (a) Mo 3d, (b) B 1s, (c) Al 2p, (d) Y 3d, (e) O 1s and (f) F 1s for the MAB and Boridene, individually.

The surface chemical bonding states of the MAB and Boridene have been probed by XPS. It analyses that along with the complete removal of Al atoms when etching $(Mo_{2/3}Y_{1/3})_2AlB_2$, essentially all Y atoms are removed (**Figure S2a**, **b**). In the spectrum of the Mo 3d region (**Figure S2c**), the Mo-B-T_z (229.6, 232.8 eV) belongs to the $Mo_{4/3}B_{2-x}T_z$ sheet, while Mo^{4+} (230.9, 234.1 eV), Mo^{5+} (232.0, 235.1 eV) and Mo^{6+} (233.2, 236.0 eV) are produced from the surface oxidation of the sample after exposure to ambient atmosphere during drying. The binding energies for the Mo-B-T_z species in the B 1s region show a shift to a lower value compared with 3D compound

MAB (**Figure S2d**), whereas the Mo-B-T_z species in the Mo 3d region show a shift to a higher BE value. Furthermore, from the XPS spectra of O 1s and F 1s of the $Mo_{4/3}B_{2-x}T_z$ (**Figure S2e**, **f**), surface terminations T_z are identified to be a mixture of -O, -OH, and -F. While the determination of the elemental ratios in the formula of the Boridene is hampered by the presence of surface oxides, combining XPS and ICP-OES analyses, with detailed information given in **Table S1** and **S2**, the chemical formula of the boride is calculated to be: $Mo_{4/3}B_{5/3\pm0.02}$

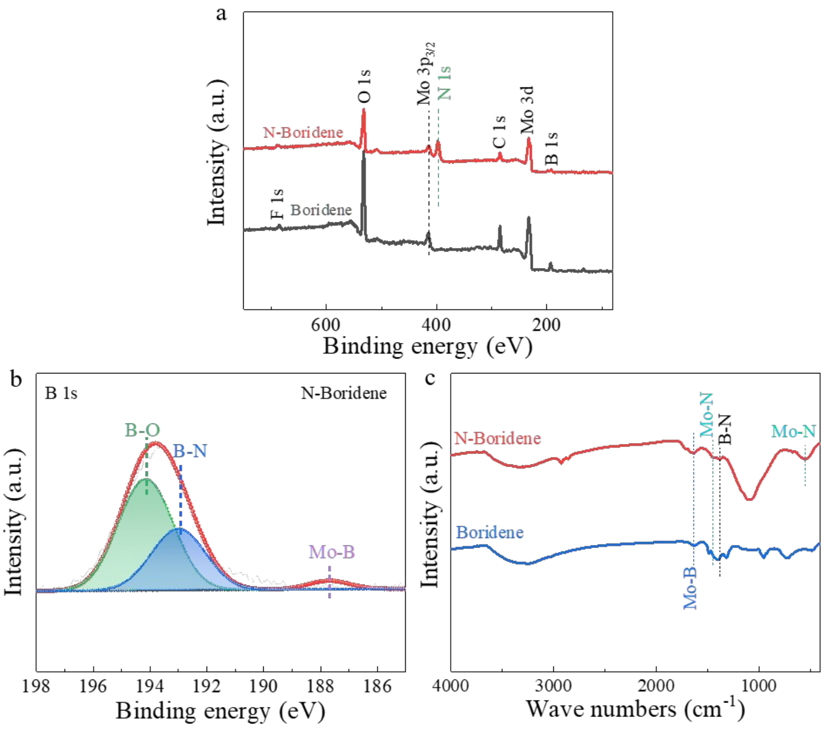

Figure S3. (a) XPS survey spectrum of the Boridene and N-Boridene. (b) XPS high-resolution diagrams of B 1s for the N-Boridene. (c) FTIR profiles of the Boridene and N-Boridene, separately. The N1s signature peaks can be observed crisply in the N-doped Boridene by comparing the XPS surveys of the reference materials (**Figure S3a**), except for Mo 3d, Mo 3p, O 1s, F 1s, and B 1s.

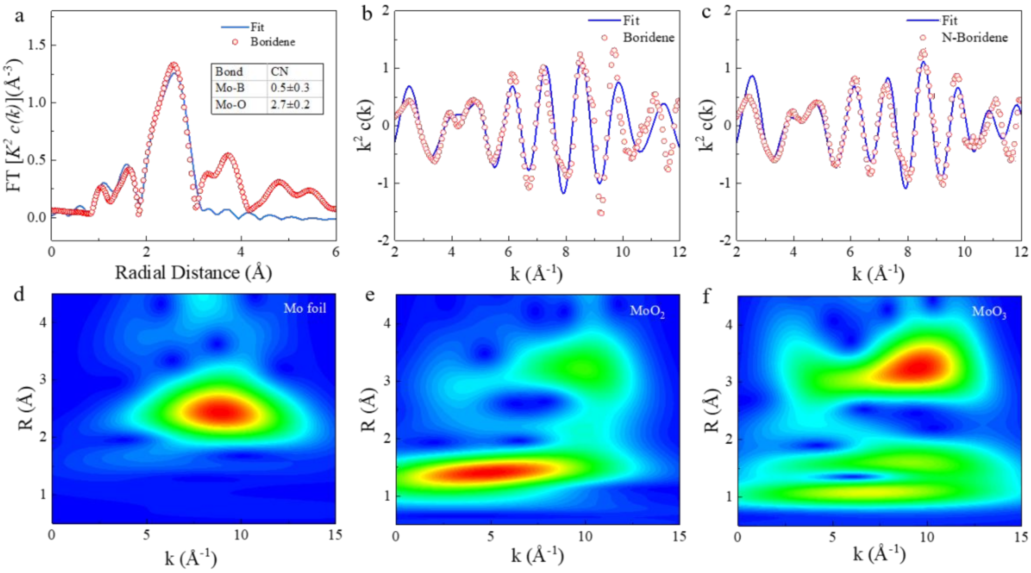

Figure S4. (a) FT-EXAFS fitting curves and (b) corresponding EXAFS k-space fitting results of the Boridene, respectively. (c) The corresponding EXAFS k-space fitting results of the N-Boridene. (d-f) WT-EXAFS plots of the Mo foil, MoO_2, and MoO_3, respectively.

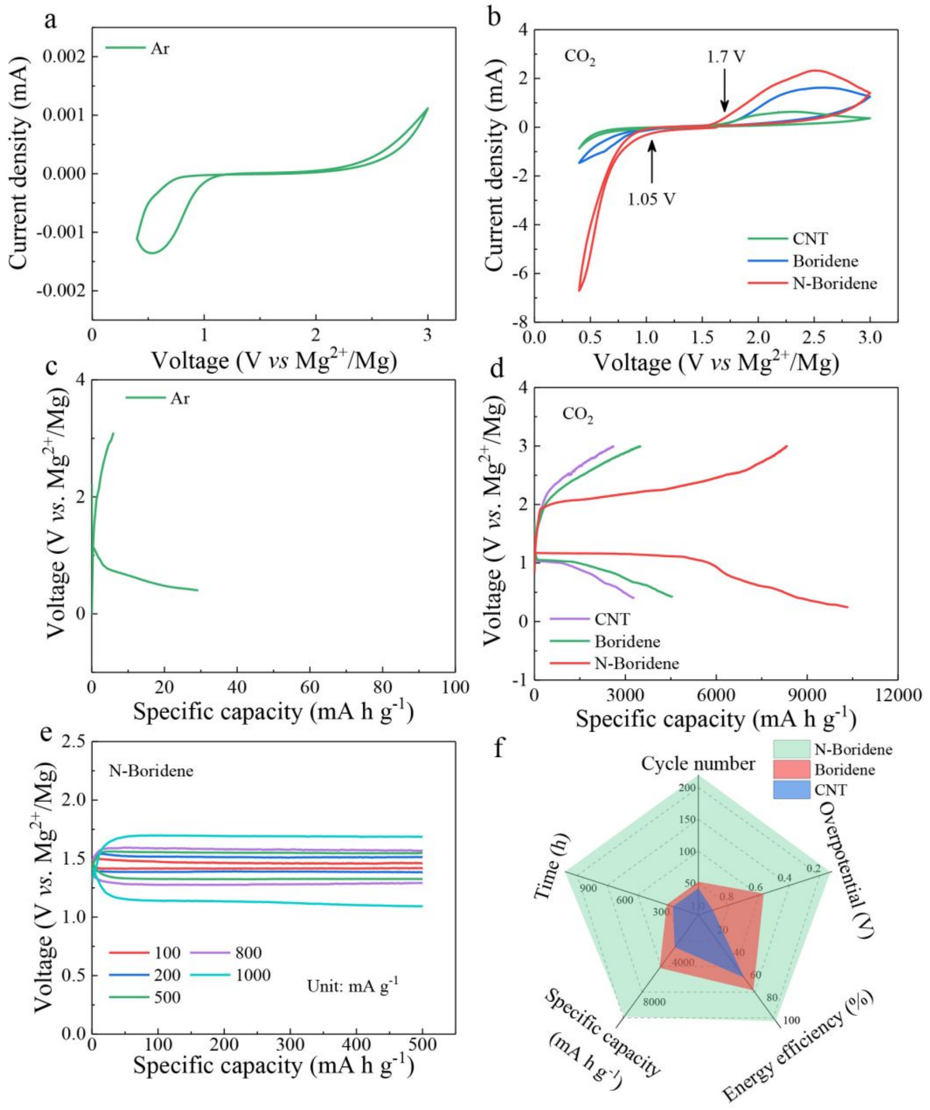

Figure S5. (a) CV curves of N-Boridene-based batteries under Ar. (b) CV curves of CNT, Boridene, and N-Boridene-based batteries under CO_2, respectively. (c) The full discharge/charge curves of N-Boridene under Ar. (d) The full discharge/charge curves of CNT, Boridene, and N-Boridene under CO_2, respectively. (e) The rate performance of N-Boridene. (f) Radar plotsof the performance properties of CNT, Boridene, and N-Boridene, respectively. The N-Boridene exhibites the negligible reactivity and a significantly low specific capacity under Ar ($\approx$ 30 mA h g^{-1} << 10300 mA h g^{-1}). This observation confirms that Mg ions do not react with Ar and there is no insertion or deinsertion of Mg ions during the cycling process.

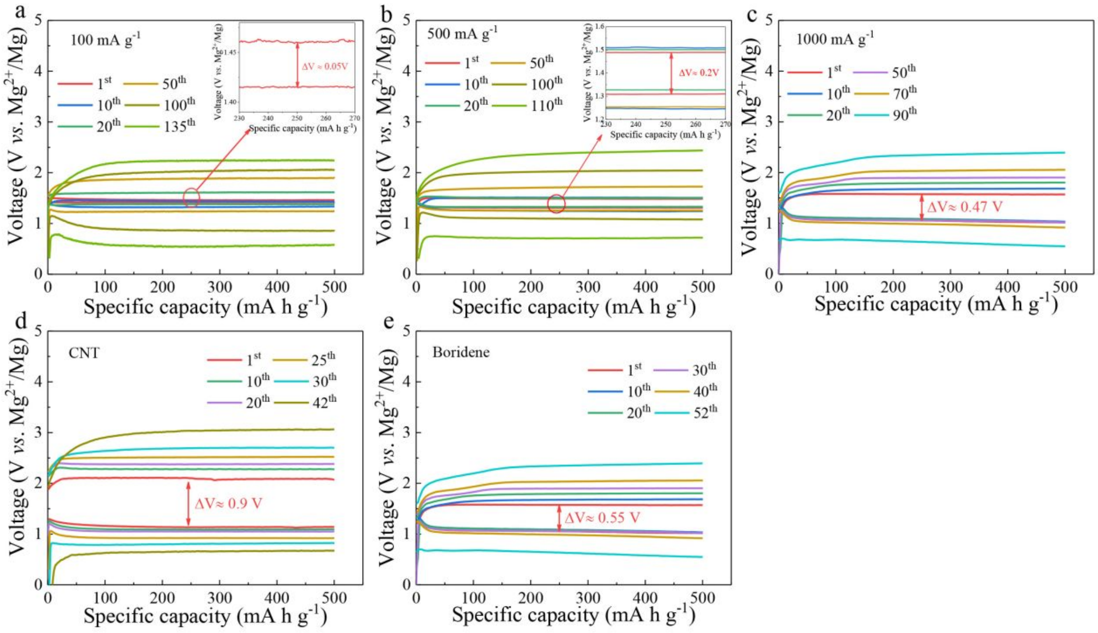

Figure S6. (a-c) Discharge/charge cycles of the N-Boridene-based Mg-CO_2 batteries at different current densities with a cutoff capacity of 500 mA h g^{-1}. (d, e) Discharge/charge cycles at 200 mA g^{-1} with a cutoff capacity of 500 mA h g^{-1} for CNT and Boridene-based Mg-CO_2 batteries, respectively.

We further examine the cycling behavior for the N-Boridene-based batteries under different current densities ranging from 100, 500, and 1000 mA g^{-1} cycled 135, 110, and 90 revolutions, severally. Whereas at the identical current density (200 mA g^{-1}), CNT, Boridene-based batteies cycled for 42 and 52 revolutions.

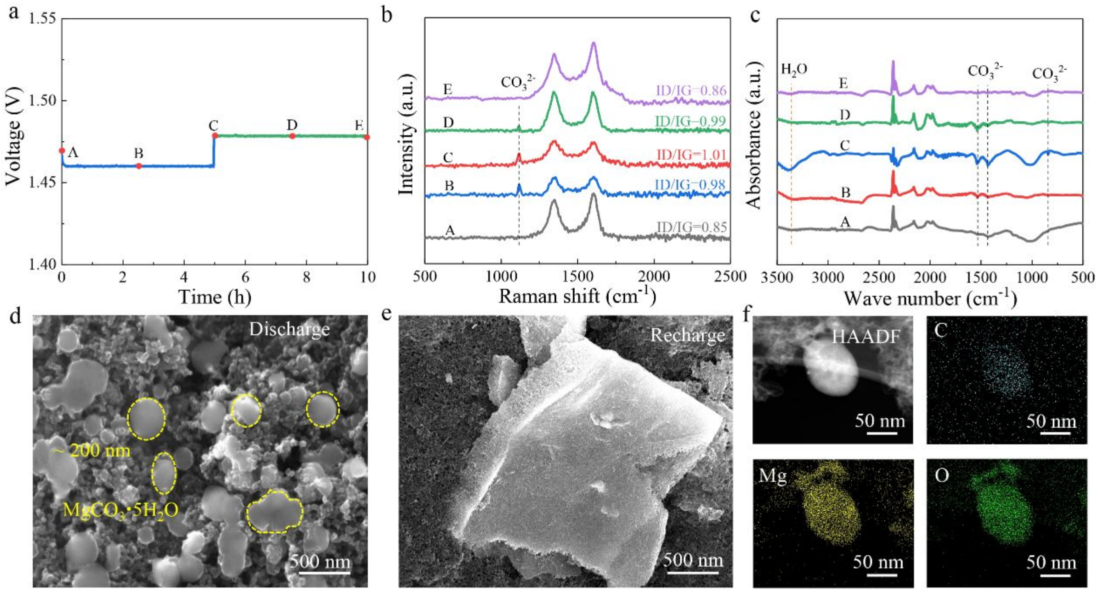

Figure S7. (a) The galvanostatic discharge/charge profiles at 100 mA g^{-1}. (b) *Ex-situ* Raman and (c) *Ex-situ* FTIR spectra at 5 selected points in one cycle. SEM images of the N-Boridene-based batteries (d) discharged and (e) recharged at 500 mA g^{-1}, respectively. (f) Elemental mapping of discharge product during the first discharge process.

The *ex-situ* Raman diagrams suggest a broad peak at 1120 cm^{-1} attributed to the vibrational mode of CO_3^{2-} in $MgCO_3·5H_2O$ gradually appeared/disappeared with the discharge/charge (**Figure S7b**), and the intensity ratio of the D band (1350 cm^{-1}) and the G band (1580 cm^{-1}) in the discharged state (1.01) is larger than that in the pristine state (0.85), demonstrating that the amorphous carbon formation. The *ex-situ* FTIR also reveals clearly the appearance/disappearance of CO_3^{2-} falling in $MgCO_3·5H_2O$ with the repetition of charging/discharging (**Figure S7c**). In this regard, the band at about 3300 cm^{-1} is ascribed to H_2O in $MgCO_3·5H_2O$.

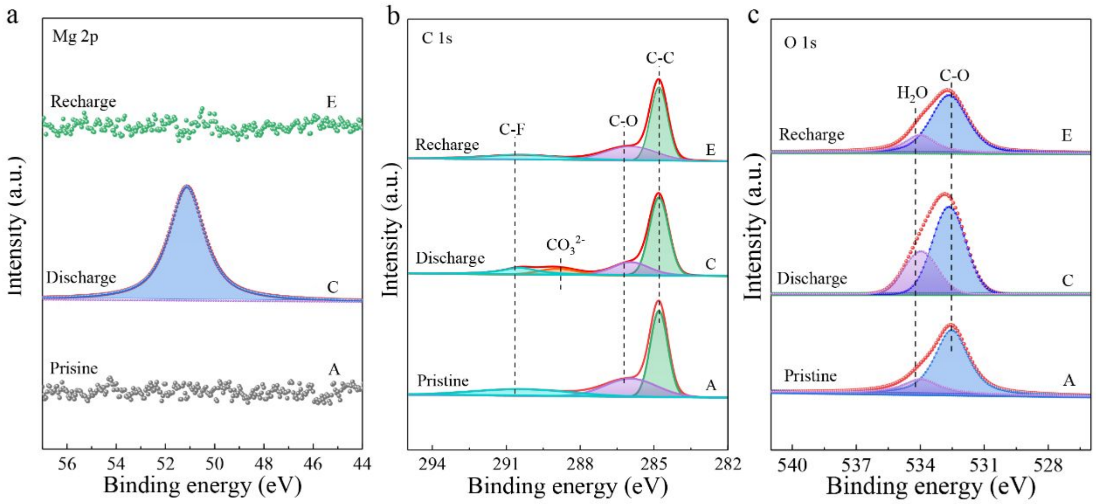

Figure S8. XPS high-resolution diagrams of Mg 2p (a), O 1s (b), and C1s (c) during the first discharge/charge process. Furthermore, the Mg 2p, C 1s, and O 1s spectra of the products peaked at about 51, 289, and 533.6 eV, respectively, corresponding to the synthesis of $MgCO_3 \cdot 5H_2O$, and inversely, the products are completely decomposed during charging.

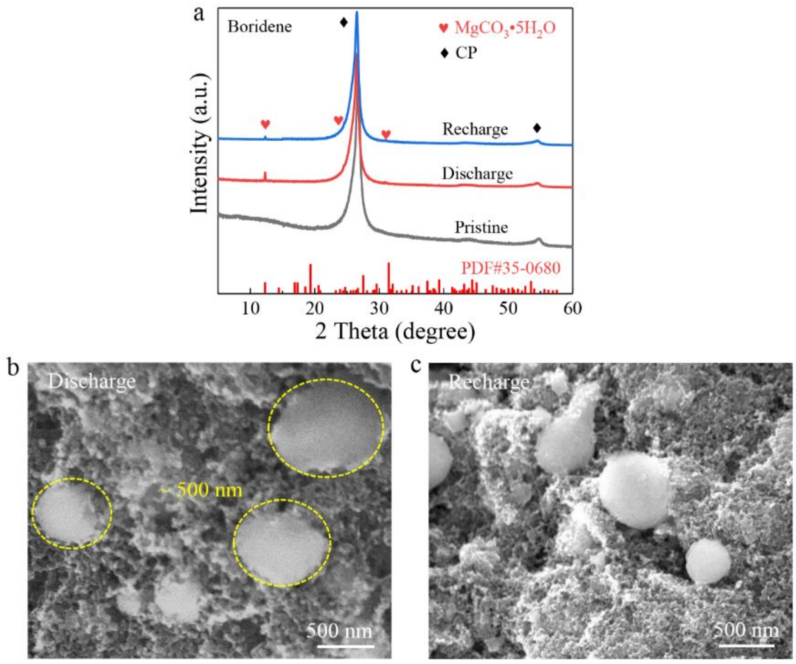

Figure S9. (a) XRD and (b, c) SEM plots of the Boridene-based Mg-CO_2 batteries during charging/discharging, respectively.

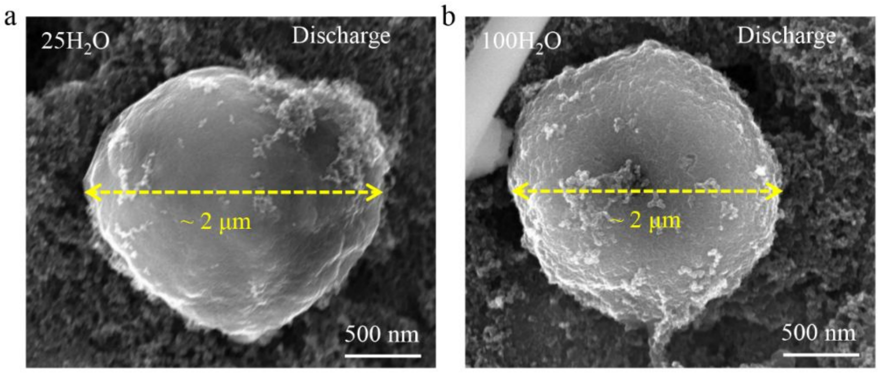

Figure S10. (a, b) SEM for 25 and 100 μL H_2O on the N-Boridene-based Mg-CO_2 batteries, individually.

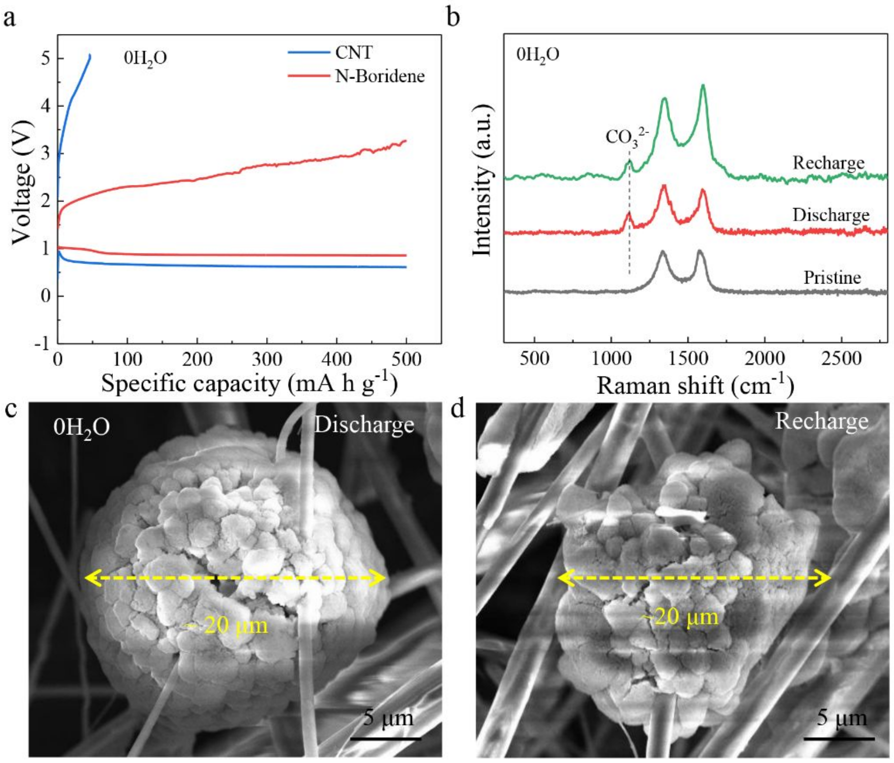

Figure S11. (a) discharge/charge profiles of the CNT and N-Boridene for 0 H_2O. (b) Raman and (c, d) SEM profiles of N-Boridene-based Mg-CO_2 battery during the discharge/charge process at 0 H_2O.

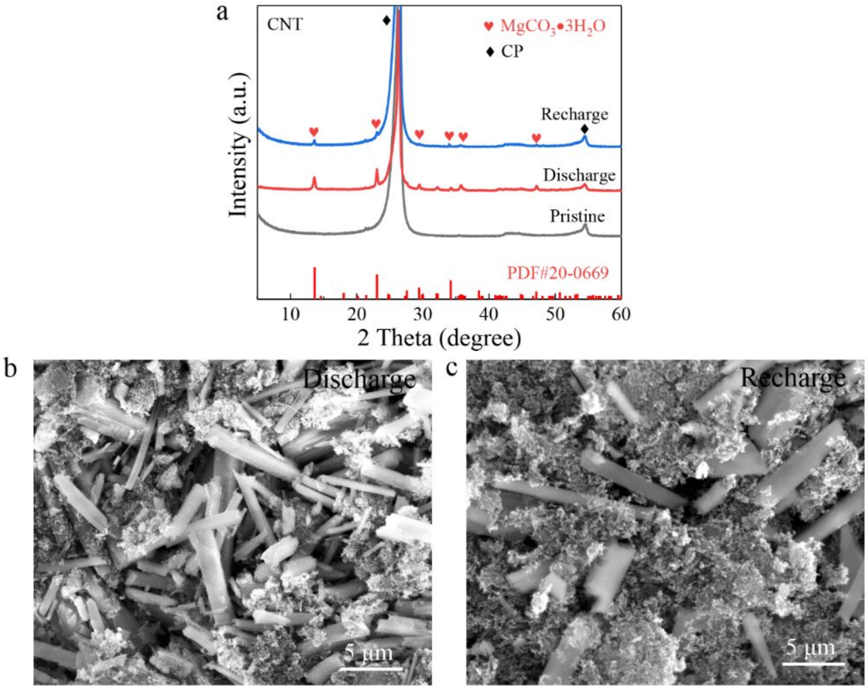

Figure S12. (a) XRD and (b, c) SEM profiles of the CNT-based Mg-CO_2 battery during the discharge/charge process at 50 H_2O.

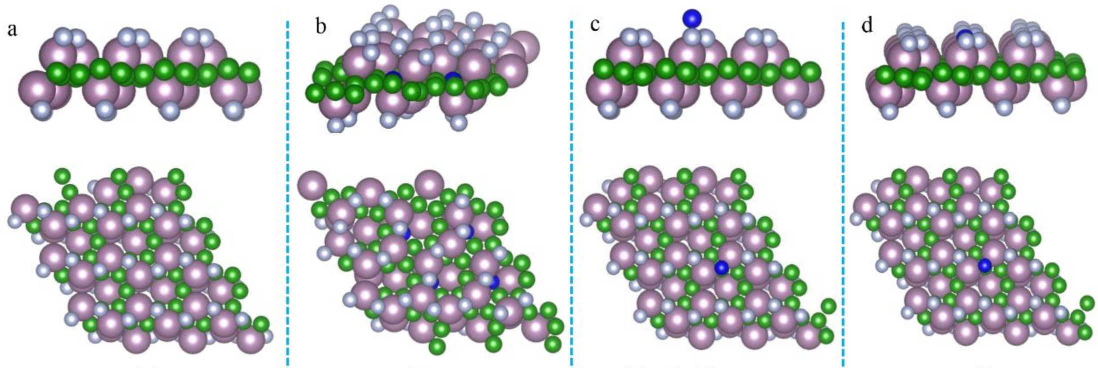

Boridene N$_{LS}$-Boridene N$_{SA}$-Boridene N$_{FS}$-Boridene

Figure S13. The sight and top views of calculated structural models for (a) Boridene, (b) N$_{LS}$-Boridene, (c) N$_{SA}$-Boridene, and (d) N$_{FS}$-Boridene, separately.

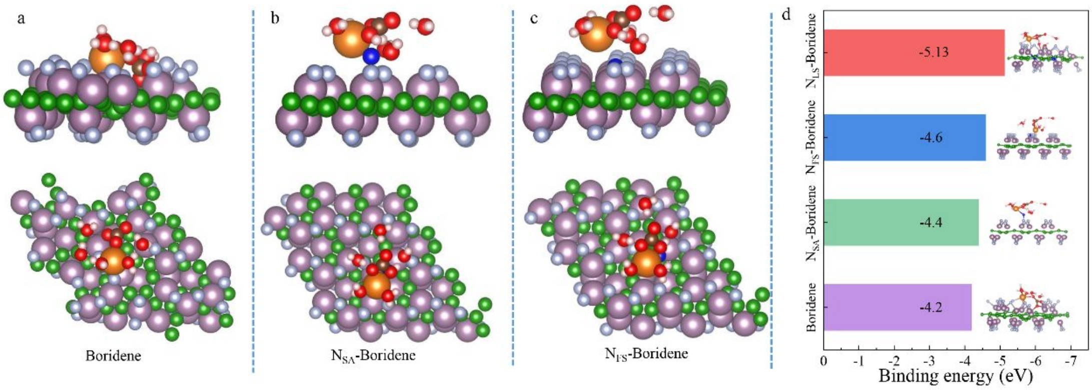

Figure S14. The sight and top views of optimized energetically favorable structures of $MgCO_3 \cdot 5H_2O$ adsorbed on (a) Boridene, (b) N_{SA}-Boridene, and (c) N_{FS}-Boridene, respectively. (d) Comparison of adsorption energies of $MgCO_3 \cdot 5H_2O$ at various positions of N atoms on Boridene substrate.

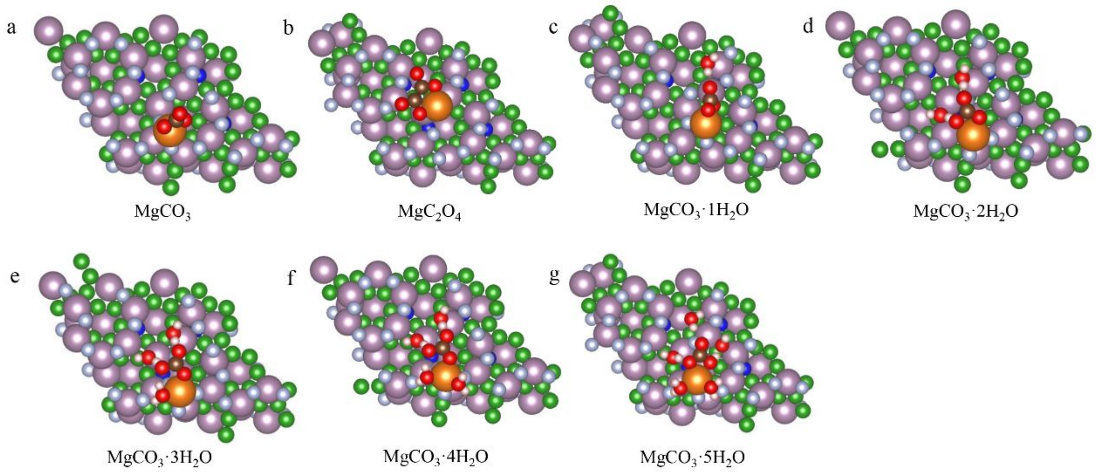

Figure S15. (a-g) Optimized structural modeling of the N_{LS}-Boridene substituents for diverse discharge products.

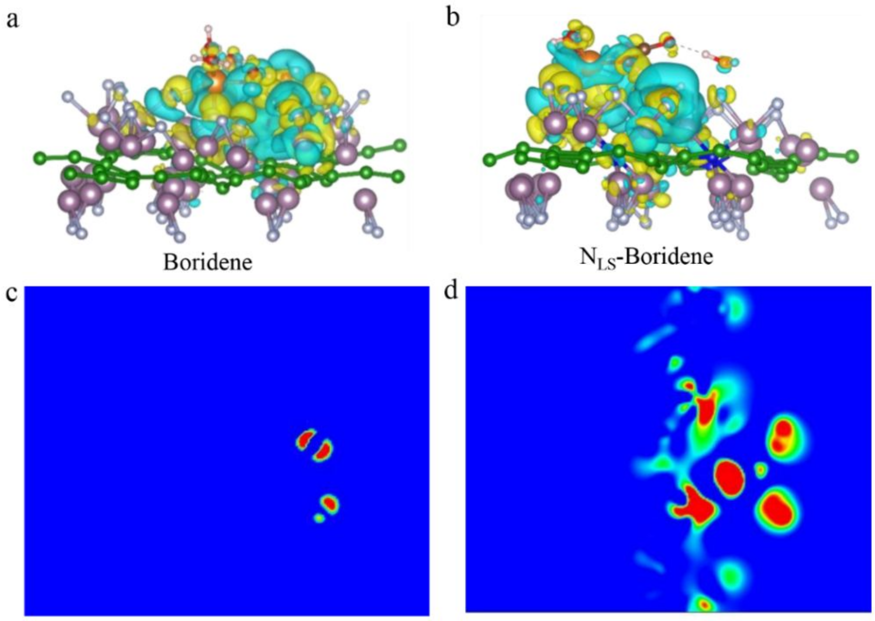

Figure S16. (a, b) Differential charge density maps of $MgCO_3\cdot 5H_2O$ by the Boridene and N-Boridene, respectively. (c, d) Charge transfer diagrams of the Boridene and N-Boridene in the (010) direction for Mg atoms.

In a differential charge density image, the integration of the charge density distribution along the z-axis direction allows us to obtain an electron quantity distribution curve, known as an electron density profile. This profile represents the number of electrons per unit volume and provides insights into the spatial distribution of electrons within the lattice structure.[35-36]

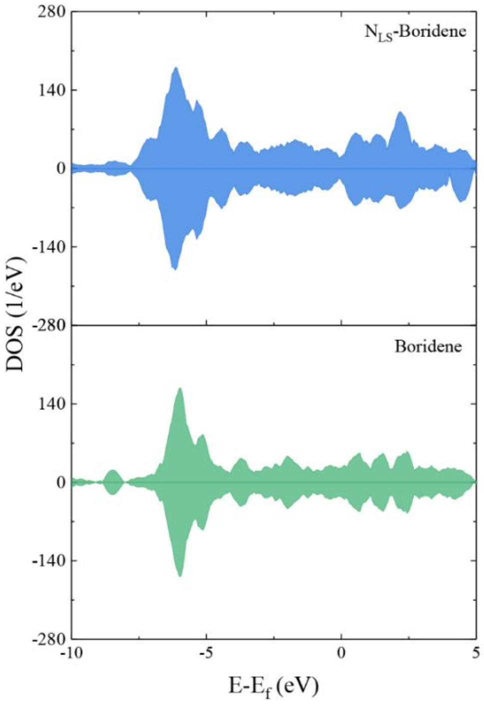

Figure S17. DOS of the Boridene and N-Boridene, respectively.

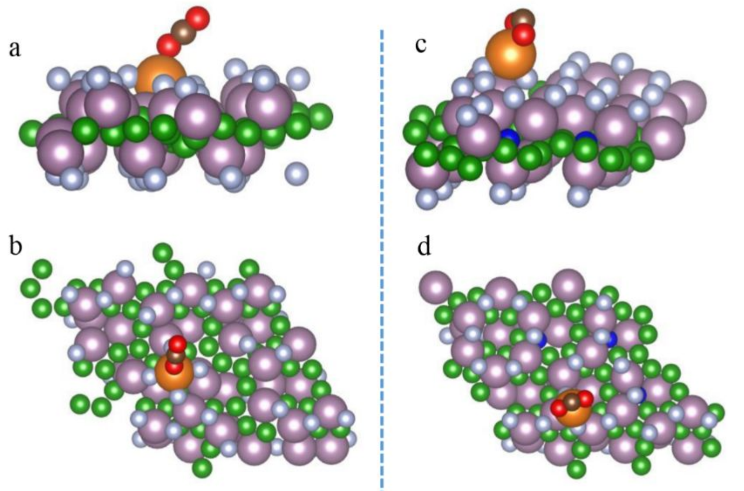

*$MgCO_2$ adsorbs on Boridene

*$MgCO_2$ adsorbs on N_{LS}-Boridene

Figure S18. The sight and top views of favorable optimization models for *$MgCO_2$ adsorption on (a, b) Boridene and (c, d) N_{LS}-Boridene, respectively.

References

[1] G. Kresse, J. Furthmüller, *Phys. rev. B* **1996**, *54*, 11169.

[2] P. E. Blöchl, *Phys. Rev. B* **1994**, *50*, 17953.

[3] J. P. Perdew, K. Burke, M. Ernzerhof, *Phys. Rev. Lett.* **1997**, *77*, 3865.

[4] S. Grimme, J. Antony, S. Ehrlich, H. Krieg, *J. Chem. Phys.* **2010**, *132*, 154104.

[5] J. Yu, M. Zeng, J. Zhou, H. Chen, G. Cong, H. Liu, M. Ji, C. Zhu, J. Xu, *Chem. Eng. J.* **2021**, *426*, 130765

[6] S.-Y. Liao, S.-F. Cui, Y.-Z. Li, W.-X. Cheng, X.-W. Huang, J. Zhang, T.-T. Cui, X.-G. Shu, Y.-G. Min, *Electrochimica Acta* **2022**, *410*, 139989.

[7] Y. Xia, L. Que, F. Yu, L. Deng, Z. Liang, Y. Jiang, M. Sun, L. Zhao, Z. Wang, *Nano-Micro Lett.* **2022**, *14*, 143.

[8] X. Chen, X. Zhai, J. Hou, H. Cao, X. Yue, M. Li, L. Chen, Z. Liu, G. Ge, X. Guo, *Chem. Eng. J.* **2021**, *420*, 129832.

[9] Z. Chen, J. Cao, X. Wu, D. Cai, M. Luo, S. Xing, X. Wen, Y. Chen, Y. Jin, D. Chen, Y. Cao, L. Wang, X. Xiong, B. Yu, *ACS Appl. Mater. Interfaces* **2022**, *14*, 12223.

[10] H. Xu, R. Zheng, D. Du, L. Ren, X. Wen, X. Wang, G. Tian, C. Shu, *Small* **2022**, *19*, 2206611.

[11] W. Bao, L. Liu, C. Wang, S. Choi, D. Wang, G. Wang, *Adv. Energy Mater.* **2018**, *8*, 1702485.

[12] C. Lu, L. Yang, B. Yan, L. Sun, P. Zhang, W. Zhang, Z. Sun, *Adv. Funct. Mater.* **2020**, *30*, 2000852.

[13] A. Amiri, Y. Chen, C. Bee Teng, M. Naraghi, *Energy Storage Mater.* **2020**, *25*, 731.

[14] Y. Yoon, M. Lee, S. K. Kim, G. Bae, W. Song, S. Myung, J. Lim, S. S. Lee, T. Zyung, K. S. An, *Adv. Energy Mater.* **2018**, *8*, 1703173.

[15] Z. Fan, C. Wei, L. Yu, Z. Xia, J. Cai, Z. Tian, G. Zou, S. X. Dou, J. Sun, *ACS Nano* **2020**, *14*, 867.

[16] Y. Wen, T. E. Rufford, X. Chen, N. Li, M. Lyu, L. Dai, L. Wang, *Nano Energy* **2017**, *38*, 368.

[17] P. Wang, Y. Ren, R. Wang, P. Zhang, M. Ding, C. Li, D. Zhao, Z. Qian, Z. Zhang, L. Zhang, L. Yin, *Nat. Commun.* **2020**, *11*, 1576.

[18] Z. Lian, Y. Lu, S. Zhao, Z. Li, Q. Liu, *Adv. Sci.* **2023**, *10*, 202205975.

[19] R. Gao, X. Liang, P. Yin, J. Wang, Y. L. Lee, Z. Hu, X. Liu, *Nano Energy* **2017**, *41*, 535.

[20] Z. Hu, Y. Xie, D. Yu, Q. Liu, L. Zhou, K. Zhang, P. Li, F. Hu, L. Li, S. Chou, S. Peng, *ACS Nano* **2021**, *15*, 8407.

[21] J. Zhou, X. Li, C. Yang, Y. Li, K. Guo, J. Cheng, D. Yuan, C. Song, J. Lu, B. Wang, *Adv. Mater.* **2018**, *31*, 1804439.

[22] J.-L. Ma, F.-L. Meng, D. Xu, X.-B. Zhang, *Energy Storage Mater.* **2017**, *6*, 1.

[23] L. Guo, B. Li, V. Thirumal, J. Song, *Chem. Commun.* **2019**, *55*, 7946.

[24] C. Fang, J. Luo, C. Jin, H. Yuan, O. Sheng, H. Huang, Y. Gan, Y. Xia, C. Liang, J. Zhang, W. Zhang, X. Tao, *ACS Appl. Mater. Interfaces* **2018**, *10*, 17240.

[25] X. Hu, P. H. Joo, E. Matios, C. Wang, J. Luo, K. Yang, W. Li, *Nano Lett.* **2020**,

20, 3620.

[26] K. Hu, L. Qin, S. Zhang, J. Zheng, J. Sun, Y. Ito, Y. Wu, *ACS Energy Lett.* **2020**, *5*, 1788.

[27] W. Zhang, C. Hu, Z. Guo, L. Dai, *Angew. Chem. Int. Ed.* **2020**, *59*, 3470.

[28] Y. Lu, Y. Cai, Q. Zhang, Y. Ni, K. Zhang, J. Chen, *Angew. Chem. Int. Ed.* **2021**, *60*, 9540.

[29] J. Xie, X. Wang, J. Lv, Y. Huang, M. Wu, Y. Wang, J. Yao, *Angew. Chem. Int. Ed.* **2018**, *57*, 16996.

[30] V. Rasupillai Dharmaraj, A. Sarkar, C.-H. Yi, K. Iputera, S.-Y. Huang, R.-J. Chung, S.-F. Hu, R.-S. Liu, *ACS Appl. Mater. Interfaces* **2023**, *15*, 9675.

[31] K. L. Ng, K. Shu, G. Azimi, *iScience* **2022**, *25*, 104711.

[32] C. Zhang, A. Wang, L. Guo, J. Yi, J. Luo, *Angew. Chem. Inter. Ed.* **2022**, *61*, e202200181

[33] W. Liu, N. Wang, Y. Wu, Q. Zhang, X. Chen, Y. Li, R. Xu, *Small* **2023**, 2306576.

[34] W. Liu, X. Sui, C. Cai, H. Huang, R. Xu, D. Geng, M. Chen, J. Lu, *Adv. Energy Mater.* **2022**, *12*, 2201675.

[35] J. Lee, J. Kim, S. Park, D. Kim, *Energy Storage Mater.* **2023**, *54*, 330.

[36] R. Seneviratne, G. Coates, Z. Xu, C. E. Cornell, R. F. Thompson, A. Sadeghpour, D. P. Maskell, L. J. C. Jeuken, M. Rappolt, P. A. Beales, *Small* **2023**, *19*, 2206267.